Formation of microbial organic carbonates during the Late Jurassic from the Northern Tethys (Amu Darya Basin, Uzbekistan): implications for Jurassic anoxic events.

Mehdi Carmeille, Raphaël Bourillot, Pierre Pellenard, Victor Dupias, Johann Schnyder, Laurent Riquier, Olivier Mathieu, Marie-Françoise Brunet, Raymond Enay, Vincent Grossi, et al.

Formation of microbial organic carbonates during the Late Jurassic from the Northern Tethys (Amu Darya Basin, Uzbekistan): Implications for Jurassic anoxic events

Mehdi Carmeille[a], Raphaël Bourillot[a], Pierre Pellenard[b], Victor Dupias[b], Johann Schnyder[c], Laurent Riquier[c], Olivier Mathieu[b], Marie-Françoise Brunet[c], Raymond Enay[d], Vincent Grossi[d], Cécile Gaborieau[e], Philippe Razin[a], Pieter T. Visscher[b, f]

[a] EA 4592 Géoressources & Environnement, ENSEGID, Bordeaux INP, 1, allée F. Daguin, 33607 Pessac Cedex, France
[b] UMR CNRS 6282 Biogéosciences, Université de Bourgogne Franche-Comté, 6, Bd Gabriel, 21000 Dijon, France
[c] Sorbonne Université, CNRS-INSU, Institut des Sciences de la Terre de Paris, iSTeP, 4 place Jussieu, 75005 Paris, France
[d] LGL-TPE-Laboratoire de Géologie de Lyon – Terre, Planètes, Environnement, UMR CNRS 5276, Université Claude Bernard, Lyon 1, 2, rue Raphaël Dubois, 69622 Villeurbanne Cedex, France
[e] I2M, UMR CNRS 5295, Esplanade des Arts et Métiers, 33405 Talence Cedex, France
[f] Department of Marine Sciences, University of Connecticut, 1080 Shennecossett Road, Groton, CT 06340, USA.

ABSTRACT

The Late Jurassic was a period of major global carbon cycle perturbations with episodes of anoxia leading to regional accumulation of organic matter in sediments worldwide. The Tubiegatan section (SW Gissar Mountains, Uzbekistan) located in the Northern Tethys, shows atypical organic-rich limestone and marl deposits (up to 6% of total organic carbon) marked by pronounced negative excursions of $\delta^{13}C_{carb}$ (amplitude of *ca.* 12‰) and $\delta^{13}C_{org}$ (amplitude of *ca.* 4‰) recorded during the Middle Oxfordian (Transversarium Zone). A transdisciplinary approach including sedimentology, palynofacies characterization, mineralogy, organic and inorganic geochemistry was carried out to elucidate the origin of these organic-rich deposits. Highest TOC are measured in nodular limestones, and lowest $\delta^{13}C_{carb}$ values in thinly laminated facies consisting in alternances of infra-millimeter-thick organic and carbonate laminae. In the latter, the presence of organic-carbonate peloids and of possible remnants of exopolymeric substances associated with clay indicate that these structures are probably mineralized laminated benthic microbial mats (i.e., stromatolites). Rock-Eval pyrolysis coupled to palynofacies analyses point to a dominant altered marine organic matter of probable algal/microbial

origin, with subordinate continental phytoclasts inputs in the upper part of the organic-rich interval. Trace elements (U/Th, V/Cr and Mo/Al ratios) indicate two anoxic episodes coinciding with the highest TOC, punctuated by dysoxic periods. Such O_2-depleted conditions have allowed the preservation and probably the development of anaerobic microbial communities in the microbial mats. In these latter, sulfate reduction probably had a significant contribution to the production of carbonates, which would explain the precipitation of pyrite and the relatively low $\delta^{13}C_{carb}$ values. The progressive decrease then disappearance of kaolinite from the base of the organic-rich interval, is interpreted as a progressive aridification of the Amu Darya Basin during the Transversarium Zone, culminating with the progradation of a large-scale gypsum sabkha overlying the organic deposits. Overall, the organic-rich deposits could record the onset of the disconnection of the Amu Darya Basin from the open sea to the south, induced by compression and subsequent uplifts in the Afghan and Central Iranian blocks. The elevated evaporation, coupled with the presence of hydrological barriers (such as coral reefs) could have led to the formation of local to regional anoxic conditions in the Amu Darya Basin. Similar microbial organic accumulations are recently known throughout the Tethys (e.g., Arabian Plate, Western Europe) and from other oceans (e.g., Central Atlantic, Pacific) during the Late Jurassic, suggesting common controlling factors. The increase of organic matter storage worldwide coupled with potential methane release could have in turn induced major perturbations of the carbon cycle during the Oxfordian-Kimmeridgian interval. The relatively shallow anoxia model proposed in this study contrasts with the well-known organic carbon-rich pelagic models proposed for the Jurassic anoxia (e.g., Toarcian, Kimmeridgian) and Cretaceous OAEs.

Keywords: Late Jurassic, Amu Darya Basin, microbial/laminated sediments, organic-rich carbonates, anoxia, stable isotopes

1. INTRODUCTION

The Late Jurassic is a period marked by multiple anoxic events (e.g., Trabucho-Alexandre et al., 2012; Martinez & Dera, 2015). More specifically, the Oxfordian and Kimmeridgian Stages are characterized by episodes of regional anoxia resulting in the accumulation and preservation of organic matter (OM)

58 in several sedimentary formations throughout the world, e.g., the Staffin Shale Fm. (Middle Callovian–
59 Lower Kimmeridgian, Isle of Skye, Scotland; Pearce et al., 2005), the Knollenkalk Fm. (Middle
60 Oxfordian, Jura, Switzerland; Rais et al., 2007), La Manga Fm. (Middle–Upper Oxfordian, Neuquen
61 Basin, Argentina; Palma et al., 2015), the Hanifa Fm. (Oxfordian–Lower Kimmeridgian, Central
62 Arabian Basin, Saudi Arabia; Droste, 1990; Vahrenkamp et al., 2015), the Smackover Fm. (Oxfordian–
63 Kimmeridgian, Gulf Coast, USA; Oehler, 1984), the Spiti Shale Fm. (Oxfordian–Berriasian, Malla
64 Johar, India; Jain et al., 1984), the Akkuyu Fm. (Lower Kimmeridgian–Tithonian, Taurus Mountains,
65 Turkey; Baudin et al., 1999), the Kimmeridge Clay Fm. (Kimmeridgian-Tithonian, Dorset, UK;
66 Tribovillard et al., 1994). A large number of these organic rocks show a fine-grained laminated fabric,
67 sometimes called organic varves. This facies has been interpreted as mineralized microbial mats (or
68 stromatolites) that formed in shallow stratified, hypersaline lagoons (Bernier and Enay, 1972;
69 Tribovillard et al., 2000; Warren, 2011). Warren (2011) postulated that such laminated organic
70 sediments could also reflect pronounced seasonal salinity and nutrient variations leading to blooms in
71 primary productivity, which in turn would result in the formation of organic laminae.
72 At the global scale, the role of climate and tectonic on the multiplication of organic-rich formations
73 during the Late Jurassic is still debated. On the Arabian platform, the Hanifa and Jubaila Fms. have
74 accumulated in partially isolated and stratified intrashelf basins. In a recent review, Vahrenkamp et al.
75 (2015) link the formation of such basins to a tectonic uplift at the margin of the Arabian Plate. Based on
76 the presence of biosiliceous deposits, Eltom et al. (2017) have related the elevated organic productivity
77 in these basins to regional upwellings developing at the shelf edge. Both models may explain the
78 formation of organic sediments on large epeiric platforms (Warren, 2011). In addition, several authors
79 proposed that the increase in organic productivity and the multiple anoxia recorded during the Late
80 Jurassic could have been caused by elevated atmospheric pCO_2 due to enhanced magmatic activity at
81 oceanic ridges and in subduction zones (Jones and Jenkyns, 2001; Dera et al., 2011; Meer et al., 2014;
82 Georgiev et al., 2017).
83 In the Western Tethyan domain, the Middle-Late Oxfordian interval is characterized by elevated carbon
84 isotope values from bulk carbonate ($\delta^{13}C_{carb}$) as reported by several authors (Bartolini et al., 1999; Louis-
85 Schmid et al., 2007; Rais et al., 2007; O'Dogherty et al., 2018), interpreted as the result of

palaeoenvironmental events (e.g., major currents reorganization, climate warming, sea-level rise, higher carbonate accumulation rates). Within this overall positive $\delta^{13}C_{carb}$ interval however, during the Transversarium Zone, a marked $\delta^{13}C_{carb}$ negative excursion was reported in the Jura and the Subalpine Basin by Padden et al. (2001). A less well-dated negative excursion was also documented in the whole Western Tethyan domain at the Middle-Late Oxfordian transition both in shallow water fossils (e.g., bivalves) and in deeper benthic organisms (e.g., belemnites; Martinez and Dera, 2015). By contrast, no well-dated $\delta^{13}C$ record is available for this period in the Northern Tethys.

The Amu Darya Basin (ADB) is a vast sedimentary basin (*ca.* 400,000 km^2) of the Northern Tethys. This basin hosts the organic-rich Khodjaipak Formation, which is a major source rock for hydrocarbons (Klett et al., 2006, 2012). This formation is dated from Late Oxfordian to Kimmeridgian in age (Abdullaev, 2004 or Mordvintsev, 2015). These 10 to 30 m thick deposits have been identified in more than two hundreds boreholes on the northeastern margin of the ADB (Besnosov and Mitta, 1995; Abdullaev et al., 2010), but outcrop only at two locations in the south-west Gissar mountain range (SW Gissar). In this study, field sedimentological investigations were carried out in one of these localities (Tubiegatan, Uzbekistan). To date, no detailed sedimentological, mineralogical or geochemical study has been published on these deposits. The Khodjaipak Fm. is located near the top of the Upper Jurassic carbonates of the Kugitang Series, and could have accumulated in depressions surrounding reefal buildups formed on the contemporaneous carbonate platforms (Mirkamalov et al., 2005). However, the absence of outcrops between the organic deposits and their potential stratigraphic counterparts in the SW Gissar implies a re-evaluation of the platform to basin correlations. The presence of ammonites in the Tubiegatan section however allows herein to specify the timing of the main paleoenvironmental events occurring at this period on the northern margin of the ADB.

In this study, the Khodjaipak Fm. organic deposits are characterized through a transdisciplinary approach including sedimentology, biostratigraphy, petrography, clay mineralogy, and organic and inorganic geochemistry. Our main objectives are to (i) determine the composition and the mode of formation of such organic deposits, (ii) propose a high resolution biostratigraphic and carbon isotope stratigraphic framework for the Tubiegatan section and (iii) establish the stratigraphic relationships with the contemporaneous carbonate platform in order to specify the depositional conditions of the

Khodjaipak Fm. The resulting model will be compared to similar Upper Jurassic deposits worldwide in order to determine potential common patterns in their formation and the potential impact on carbon cycle of multiple organic carbon accumulations.

2. GEOLOGICAL SETTING

The Kugitang Series is a thick carbonate platform succession (~100–600 m) deposited on the NE margins of the ADB (**Fig. 1A**) from the Early Callovian up to the Kimmeridgian (Mirkamalov et al., 2005; Nugmanov, 2010; Carmeille et al., 2018). This series crops out in the southwestern Gissar mountain range (SW Gissar), in the northeastern part of the ADB. The Kugitang carbonate platform is subdivided into two major depositional sequences: (i) the Callovian Sequence (CS) equivalent to the Lower Kugitang Series and (ii) the Upper Jurassic Sequence (UJS) equivalent to the Upper Kugitang series (**Fig. 2**; Carmeille et al., 2018). The CS deposition begun in the Early Callovian and lasted at least until the top of the Middle Callovian (Coronatum Zone), or possibly until the Late Callovian (**Fig. 2**; Mitta, 1992). At this time, the SW Gissar was covered by a carbonate ramp. The CS ended with a major subaerial exposure surface probably associated with a hiatus. The UJS records a major reorganization of the platform. A vast low energy lagoon developed, probably protected by a barrier reef outcropping in the Kugitang area (southern part of the SW Gissar; **Fig. 1A,B**). The organic-rich deposits of the Khodjaipak Fm. could be partly time-equivalent of this barrier reef (Abdullaev, 2004). The Khodjaipak Fm. dated as Upper Oxfordian and Kimmeridgian (Abdullaev, 1999, 2004; Abdullaev and Mirkamalov, 2001) is considered as a major type-II kerogen source rock (Ulmishek, 2004). On the Chardzhou step (NE margin of the ADB; **Fig. 1A**), more than two hundred boreholes from major gas fields have drilled this formation (e.g., North Kamashi, South Alan, Ayzovat 7; Ulmishek, 2004; Mirkamalov et al., 2005; Abdullaev et al., 2010; Mordvintsev, 2015).

The Khodjaipak Fm. crops out only in two localities close to the Turkmenistan-Uzbekistan border: Tubiegatan and Gaurdak (Besnosov & Mitta, 1995; **Fig. 1B**). We did not obtain authorizations to work on the Gaurdak section, located on the Turkmen side. The focus of this study is the Tubiegatan section, located on the Uzbek side. The section exposes a 30-meter-thick limestone interval belonging to the Kugitang Series (**Fig. 2**), overlain by 10 meters of dark limestone and marl alternation (**Fig. 1C**). The

studied deposits crops out along a *ca.* 1 km wide window on the flank of an anticline, thanks to a local gliding of the overlying Irgayli Fm. gypsum (**Figs 1D and 2**).

3. MATERIALS AND METHODS

3.1. Ammonite biostratigraphy and sequence stratigraphy

A total of 14 ammonites (entire or fragments) were collected along the measured section. Six of them were determined to the species level by one of us (RE) using the standard biozonation of the NW Tethyan domain (Cariou and Hantzpergue, 1997). A sequence stratigraphic scheme was built based on Maximum Flooding Surfaces (MFSs) and Maximum Regressive Surfaces or Sequence Boundaries (SBs), following the terminology of Catuneanu et al. (2011).

3.2. Petrography

A total of 90 samples were collected. To obtain a high-resolution record, one sample was taken every 20 cm on average within the organic-rich carbonates and marls deposits. In the limestone interval (Kugitang Series), we took one sample every 1 m on average. Thin sections were prepared (polished with 0.25 µm alumina powder and impregnated with blue epoxy resin) and observed under a Nikon Eclipse Ci polarizing microscope for 50 samples allowing the characterization of microfacies. Three thin sections were examined with a FEI Quanta 250 FEG environmental scanning electron microscope, under low vacuum. One third of each thin section was etched in 10% acetic acid for 1 minute, in order to remove carbonates and have a better observation of the OM. X-ray spectral microanalyses and X-ray maps were performed using energy dispersive spectrometry (EDS, EDAX Apollo XL) at the I2M laboratory, Bordeaux, France.

3.3. Palynofacies analyses

Determination of palynofacies have been realized on 28 samples. One sample (12-E1) was almost barren of OM and thus unsuitable for palynofacies examination. The carbonate minerals were first dissolved using hydrochloric acid (HCl). Then, the residues were treated with hydrofluoric acid (HF) in order to eliminate the silicates. For each sample, two aliquots of the remaining organic residues were used to

make a non-filtered slide and a filtered slide using a 10 µm sieve mesh. The slides were then examined under an Axioplan2 Imaging Zeiss microscope. Both qualitative and quantitative observations were made. We used a simplified version of the palynofacies classifications proposed by Whitaker et al. (1992) and Tyson (2012), with some modifications by McArthur et al. (2016). The relative surface area of each classes was estimated on the filtered slides, as they allow a better observation of the relative proportions of phytoclasts and palynomorphs. Further details regarding the palynofacies method used in this study can be found in Schnyder et al. (2017). These analyses were conducted at the Institut des Sciences de la Terre de Paris (ISTeP) laboratory (Sorbonne-Université, Paris, France).

3.4. X-ray diffraction

X-ray diffraction analyses were performed at the Biogéosciences laboratory (Université Bourgogne Franche-Comté, Dijon, France) to identify and semi-quantify mineralogy of the bulk-rock (85 samples) and the <2µm clay-size fraction (80 samples). Clay minerals were identified in oriented mounts of non-calcareous clay-size fraction, following the analytical procedure of Moore and Reynolds (1989). After removing carbonate (using 2N HCl for marl and 12N HCl for limestone), clays were deflocculated by successive washing with distilled water. Particles finer than 2 µm were concentrated by centrifugation. Diffractograms were obtained using a Bruker D4 Endeavor diffractometer with CuKα radiation, LynxEye detector and Ni filter, under 40 kV voltage and 25 mA intensity. Three XRD runs were performed, after air drying (AD), ethylene-glycol solvation (EG), and heating at 490 °C for 2 h. The goniometer performed a scan from 2.5° to 28.5° 2θ for each run. Identification and semi-quantitative estimates of clay mineralogy were made according to the position and the area of the (001) basal reflections on the three XRD pattern (Moore and Reynolds, 1989). The identified clay minerals are R1 type illite/smectite mixed-layers (I/S-R1), illite, kaolinite and chlorite. Deconvolution of peak areas of kaolinite (d_{002}) and chlorite (d_{004}) was performed to discriminate both minerals using MacDiff 4.2.5 software (Petschick, 2001). Other non-clay minerals found in the bulk rock are calcite, quartz, feldspars and pyrite. Semi-quantification of these phases are performed considering mean reflexions (100% intensity) of each phase and using the $\%CaCO_3$ measured by spectrometry.

3.5. Rock-Eval pyrolysis

A total of 61 samples were analyzed by Rock-Eval pyrolysis using a Rock-Eval 6 Turbo (Vinci Technologies) at the Institut des Sciences de la Terre de Paris (ISTeP) laboratory (Sorbonne-Université, Paris, France). The following parameters were obtained (Espitalié et al., 1985; Behar et al., 2001): (i) the total organic carbon (TOC, in wt %); (ii) the hydrogen index (HI, in mgHC/g-TOC), calculated from the quantity of pyrolysable organic compounds from S2 peak released during pyrolysis, normalized to TOC values; (iii) the oxygen index (OI, in mgCO_2/g-TOC), obtained from the amounts of CO and CO_2 from S3 peak released during pyrolysis, normalized to TOC values, and (iv) the T_{max}, corresponding to the temperature recorded in the oven at the peak of hydrocarbon production during pyrolysis. Analytical precision is ± 0.1% for TOC, ± 10 mgHC/g-TOC for HI, ± 5 mg CO_2/g-TOC for OI and ± 2°C for T_{max}.

3.6. Stable isotope geochemistry ($\delta^{13}C_{carb}$, $\delta^{18}O_{carb}$, $\delta^{13}C_{org}$, $\delta^{15}N_{tot}$)

The $\delta^{13}C_{carb}$ and the $\delta^{18}O_{carb}$ (bulk carbonate fraction) were measured on 72 samples at the Biogéosciences laboratory (Université Bourgogne Franche-Comté, Dijon, France). About 50-90 µg of powder were produced by using a micro-drill to avoid crack fillings or fossils. Powder was oven-dried for 12 h at 50 °C then weighed with a Mettler Toledo XS3DU ultra-balance (30 to 60 µg, depending on %$CaCO_3$). A Kiel IV carbonate preparation device, paired with a Delta V Plus (ThermoFisher) mass spectrometer was used for isotopic analyses. Samples were dissolved at 70 °C by orthophosphoric acid, and isotopic values were calibrated by NBS-19 and Merck standard. Carbon isotopic composition is expressed in per mil (‰) V-PDB, and oxygen isotopic composition in ‰ SMOW. Replicates (every 7 samples) showed reproducibility of ± 0.07 ‰ for carbon and ± 0.1 ‰ for oxygen.

The $\delta^{13}C_{org}$ was measured on 75 samples and the $\delta^{15}N_{tot}$ was measured on 66 samples at the Biogéosciences laboratory (Université Bourgogne Franche-Comté, Dijon, France). After grinding, the carbonate minerals were dissolved using 6N HCl. The powder was then rinsed with purified water and oven-dried at 50°C before analyses. The $\delta^{13}C_{org}$ and $\delta^{15}N_{tot}$ analyses were performed using a vario MICRO cube (Elementar) elemental analyser, paired to an Isoprime (Elementar) isotope ratio mass spectrometer (EA-IRMS). The values were compared to USGS40 L-Glutamic acid ($\delta^{13}C$ = -26.39 ± 0.04 ‰; $\delta^{15}N$ = -4.5 ± 0.1 ‰) and IAEA-600 Caffeine ($\delta^{13}C$ = -27.77 ± 0.04 ‰; $\delta^{15}N$ = +1.0 ± 0.2 ‰)

international standards for $\delta^{13}C_{org}$ and $\delta^{15}N_{tot}$. The $\delta^{13}C_{org}$ and $\delta^{15}N_{tot}$ values are expressed in ‰ V-PDB and % V-AIR respectively. For each sample, replicates showed reproducibility better than ±0.3 ‰ for $\delta^{13}C$ and ±0.5 ‰ for $\delta^{15}N$.

3.7. Major and trace element geochemistry

Multi-elemental analyses were performed using ICP-AES for major elements and ICP-MS for trace elements on 23 samples at the spectrochemical laboratory of the Centre de Recherche Pétrographiques et Géochimiques (CRPG, Vandoeuvre-les-Nancy, France). The samples were prepared by fusion with $LiBO_2$ and HNO_3 dissolution. The average uncertainties are about 1% for major elements, 5% for Cr, U and V, and 10% for Co, Mo, and Ni as checked by international standards (Carignan et al., 2001).

Usually, trace elements are Al-normalized in order to dissociate the detrital and authigenic fractions. However, because of fluctuating Al concentrations (from 0.08 to 5%), the use of fraction in excess was preferred to dissociate these two fractions. As proposed by Brumsack (2006), the detrital fraction $X_{detritic}$ has been calculated using the formulae: $X_{detritic} = Al_{sample} \times (X/Al_{upper\ crust})$. The values of upper continental crust are from McLennan (2001). Then, the "excess" (non-detrital) fraction has been calculated, using the formulae $X_{xs} = X_{sample} - X_{detritic}$ for each element, which does not show strong correlations with Al and Ti, considered as elements with a detrital origin (Tribovillard et al., 2006; Collin et al., 2015).

4. RESULTS AND INTERPRETATIONS

Based on the vertical facies succession, we defined three lithostratigraphic intervals along the Tubiegatan section: (1) a lower carbonate interval; (2) an organic-rich marl and limestone unit corresponding to the Khodjaipak Fm. and (3) a second carbonate interval at the top. In terms of sequence stratigraphy, the whole succession can be interpreted as a transgressive-regressive third-order sequence with a proposed MFS located *ca.* 20 m from the basis of the section. This sequence can be subdivided into three higher frequency depositional sequences (Tu1, Tu2 and Tu3; **Fig. 3**).

4.1. Sedimentology and stratigraphy

4.1.1. Lower carbonate interval (0–30 m), Tu1 and Tu2 sequences, base of Tu3 sequence

Mudstones (F2a) and pellet-sponge spicule wackestones (F2b) predominate in the first 25 meters of the section (**Fig. 3**). Such mud and pellet-rich facies are indicative of low energy conditions (Carmeille et al., 2018), and in the absence of storm-deposits they are usually placed below the storm wave base (SWB; Wilson, 1975; Carpentier et al., 2007). The diversified photo-independent benthic associations: sponge spicules, benthic foraminifera, echinoderms and oysters, suggest a well-oxygenated bottom water located below the photic zone. Ammonite imprints were also locally observed at the surface of beds. The micritized ooids (F2e) observed at 14 and 29 m could be exported from the inner platform during shallowing-upward trends. Dolomitized *Thalassinoides* burrowed horizons (**Fig. 4B,C**) reflect the formation of firmgrounds possibly recording a decrease in the sedimentation rate and water depth (Carmeille et al., 2018). Consequently, we placed two 4th order sequence boundaries (14 m and 27 m) within these burrowed intervals (**Fig. 3**). The occurrence of *Perisphinctes* (*Kranaosphinctes*) sp. would place the top of Tu1 and the basis of Tu2 in the Oxfordian. The dolomitized *Thalassinoides* burrows at the top of Tu2 (25 to 27 m) are locally filled with diagenetic iron oxides.

The overlying carbonate strata (27 to 30 m) are characterized by serpulids and benthic foraminifera (including Lituolids) packstone (F2c) and *Crescentiella morronensis* and brown foraminifera oncoids pack- to floatstone (F2d). They are placed within the sequence Tu3. The last bed of the lower carbonate interval shows a significant fossil concentration: ammonites, belemnite rostra, oysters and benthic foraminifera (F1d). This fossil association indicates the persistence of a good oxygenation of the whole water column. A hardground develops at the top of this bed, likely reflecting a decreased sedimentation rate. Overall, the lower carbonate interval was mostly deposited below SWB and shows evidence for a well-oxygenated water column.

4.1.2. The Khodjaipak Fm. (30–40 m), Tu3 sequence

From 30 to 40 m (**Fig. 3**), the series is dominated by organic-rich marls to siltstones (F1a) and microbial boundstones (F1c), interbedded with black nodular mudstones (F1b) and tempestites (F1d). Millimeter-

laminated dark to brown marls to siltstones (F1a; **Fig. 4D**) containing ammonites and entire bivalves in life position are characterized by TOC values comprised between 0.4% and 4%. The black nodules (F1b) found in these dark to brown marls show the highest TOC values, reaching 6% (**Fig. 4E).** F1c consists of sub-millimetric alternations of carbonate and organic laminae (**Fig. 5A-C**), with TOC values comprised between 0.5% and ~2% (**Fig. 3**). Sponge spicules, benthic (rotaliids: *Lenticulina, Rheinholdella*?) and planktonic foraminifera are locally concentrated in thin laminae (**Fig. 5D**). Diagenetic anhydrite pseudomorphs and dolomite rhombs are observed in this facies (**Fig. 5B**). F1d corresponds to dark shell beds (**Fig. 4F**) with moderate TOC (0.8-1.6%). The skeletal elements consist of well-preserved, disarticulated and oriented brachiopod and bivalve shells (e.g., *Trichites*, pectinids, oysters), which are associated with abundant rotaliid foraminifera (identical to those observed in F2c), sponge spicules and rare echinoderm fragments floating in a dark-micritic matrix. The ammonite *Subdiscosphinctes (Subdiscophinctes)* cf. *richei* De Riaz */mindowe* Siemiradzki precisely dates this interval to the Schilli Subzone (Transversarium Zone, Middle Oxfordian; **Fig. 3**). The suggested depositional environment for these organic carbonates is discussed in details in Section 5.3.1.

4.1.3. Upper carbonate interval and chicken wire gypsum (40–43m), Tu3 sequence

The section is capped by a 2-m-thick carbonates interval characterized by peloid and fine micritized ooid pack- to grainstone (F3a) and stromatolitic boundstone (F3b). These carbonates are overlain by chicken-wire gypsum, typical of sabkha deposits, whose exact thickness cannot be determined (F4; **Fig. 3**).

4.2. Petrography of microbial organic carbonates

The organic-rich, laminated microbial boundstone (F1c; **Fig. 5A,B**) is abundant in the Khodjaipak Fm. (**Fig. 3**). This facies displays two main microfabrics: (i) 10 µm to 1 mm thick organic and micritic/microsparitic laminae that alternate with (ii) 100s of microns to 3 mm thick peloidal laminae (**Fig. 5C**). Macroscopically (**Fig. 5A**), the carbonate-rich beige laminae and the dark organic-rich laminae alternation are very similar to the intertidal microbial mats observed in the modern Abu Dhabi sabkha (Lokier et al., 2017). Microspar and micrite are abundant in both dark and clear laminae (**Fig. 5E**). Foraminifera (**Fig. 5D**) and sponge spicules rich laminae were probably formed through trapping

and binding processes (e.g., Bouton et al., 2016). OM has two main loci: (i) yellowish to dark aggregates are observed within peloids (**Fig. 5C**) and microspar crystals (**Fig. 5F**); similar coccoid bacteria clusters are documented in modern hypersaline lagoon microbialites (e.g., Dupraz et al., 2004); (ii) a thin dark lining occurs between spar crystals (**Fig. 5E,F**) and sometimes impregnates the wall of foraminifera and other microfossils (**Fig. 5D**). Three samples were observed under SEM and analysed with EDS (**Fig. 6**). Peloids develop within an alveolar OM network (**Fig. 6A-C**), very close to modern microbial mats exopolymeric substances (EPS; e.g., Dupraz et al., 2004; Pace et al., 2018). Platy clay minerals characterized by high content in Al, and possibly of detrital origin, are associated with OM (**Fig. 6D**). The clay-OM complexes include very small sulfur globules (mostly <1µm in diameter). Some samples show a significant proportion of iron oxides associated with organic carbon (**Fig. 6E,F**).

4.3. Bulk and clay mineralogy

Carbonates predominate in the lower and upper carbonate intervals (90-100% of $CaCO_3$; **Fig. 3**). In the Khodjaipak Fm., the proportion of calcium carbonate and quartz fluctuates: microbial laminites (F1c) contain up to 92% of $CaCO_3$, while brown marls to siltstones contain up to 50% of quartz. The proportion of clay minerals in the bulk rock is overall low (< 1%) in the lower and upper carbonate intervals. The percentage increases in the Khodjaipak Fm., where clay accounts for up to 8% of the bulk rock. Pyrite content is relatively low (< 0.5%) in the lower and upper carbonate intervals and reaches 1% for several horizons within the Khodjaipak Fm. (**Fig. 3**).

We subdivide the section into five intervals based on the clay mineral association (intervals 1 to 5; **Fig. 3**). From 1 m to 20 m, the relative percentage of the various clay minerals is relatively constant: illite predominates with values comprised between 55 and 75%, followed by R1 type illite/smectite mixed-layers (I/S-R1; 20-40%), kaolinite (0-10%) and chlorite (0-5%). A second interval (20 to 30 m) is characterized by an increase of kaolinite (up to 40% at 27.5 m) followed by a slight decrease, at the expense of illite (approximately 40 to 70%). Chlorite displays similar variations as kaolinite, but represents a smaller proportion of the clay assemblage (< 15%). I/S-R1 content ranges between 15 and 25%. The third interval (30 to 36 m), starting at the basis of the Khodjaipak Fm., is marked by highest content and significant fluctuations of kaolinite, with two peaks at 31 and 31.7 m, reaching 65% and

63% respectively, and the decrease of illite and chlorite contents. From 36 m to 40 m (interval 4), kaolinite and chlorite are absent, IS-R1 varies between 0 and 30%, while illite remains the dominant clay mineral.

4.4. Rock Eval pyrolysis

TOC values range from 0wt% (peloidal pack- to µgrainstone, F3a) to 6wt% for the thinly laminated black limestones with nodules (F1b; **Figs 3 and S1**). The lower carbonate interval does not contain organic carbon. Within the Khodjaipak Fm., the higher TOC values were measured in limestones (2.0% on average in F1b, F1c and F1d) while lower TOC values (avg. 0.5%) characterized marls and claystone (F1a; **Fig. S1**). The TOC is relatively low (0-1.8%) from 30 to 33.5 m, then increases from 33.5 to 34.5 m and remains at fluctuating but relatively high values (0.7-6%) up to 38 m to finally progressively decrease to 0% in the upper carbonate interval.

Throughout the dark organic-rich deposits interval, the T_{max} values form two groups (**Fig. 7**). Most of the values range between 440 and 465°C, characterizing a mature OM which has reached the oil window, while a second group shows values comprised between 515 and 540°C (**Fig. 7**), indicating the gas window (Tyson, 1995). The HI values obtained in the Khodjaipak Fm. range from 7 to 142 mgHC/g-TOC. Along the studied section, the HI fluctuates rapidly between values above 100 mgHC/g-TOC and below 50 mgHC/g-TOC (**Fig. 7**). These observations as well as the high values of T_{max} may be the reflection of a degradation of the OM. The HI / T_{max} relation (**Fig. 7**) points to a Type III (terrestrial OM) to Type IV OM, the latter characterizing a highly altered organic material (generally oxidized) whose biological origin is not determinable (Baudin et al., 2007). However the burial of OM selectively removes hydrogen-rich OM and induces a depletion of IH values (Espitalié et al., 1985). Consequently, it is probable that at least a part of the OM was originally of Type II (marine OM) and was subsequently thermally degraded. Therefore, the Rock-Eval analysis is most probably not conclusive regarding the OM origin, and palynofacies data are used to discriminate OM sources (see section 4.5).

4.5. Palynofacies

The studied palynofacies comprise nine classes of components (**Fig. 8**), following a simplified version of the palynofacies classifications published by Whitaker et al. (1992), Tyson (1995) and McArthur et al. (2016): (i) opaque phytoclasts, (ii) translucent phytoclasts, (iii) dark structureless organic matter (DSOM), (iv) well-preserved wood fragments (WPWF), (v) amorphised degraded brown wood (DBW) and dark amorphous organic matter (AOM) flakes with rectangular shapes, (vi) pollen grains and spores, (vii) orange to dark AOM flakes, (viii), dinoflagellate cysts, and (ix) foraminiferal linings. The translucent phytoclasts correspond to flat, pale brown to transparent fragments including leaf cuticles and aqueous plant remains. DSOM are dark brown to orange fragments originating from degraded products of plant debris and humic gel. WPWF are dark-brown fragments showing preserved wood structures (tracheids, lignified walls). DBW and rectangular AOM are dark-brown to yellow, flat, with gelified to amorphized structures. These particles partly derive from terrestrial wood fragments and/or from lignified parts of aqueous plants that are heavily degraded, gelified and amorphized in an aqueous environment. Similar amorphization and gelification processes due to bio-degradation of terrestrial or aquatic plant tissues have been reported in peat and aquatic marshes environments (Laggoun-Défarge et al., 1999; Sebag et al., 2006; Storme et al. 2012). The vertical evolution of the relative percentage of these classes is represented on **Figure 8**.

AOM is largely predominant in the Tubiegatan section, accounting for more than 75% in the countings in 18 out of 27 samples (**Fig. 8**). AOM is generally interpreted as being of microbial and/or algal origin (e.g., Tyson, 1995) and a mostly marine origin of the AOM is probable in the Tubiegatan section. However, dark AOM particles with rectangular shape observed at some stratigraphic levels between 34.8 and 38.8 m are associated with DBW. Therefore, this type of AOM could be different from the rest of the observed AOM, and is here interpreted as most probably originating from degraded terrestrial and/or aquatic macrophytes tissues. A second characteristic of the palynofacies from Tubiegatan is the common occurrence of -at least partly- terrestrial-derived materials, such as opaque and translucent phytoclasts, DSOM, WPWF, amorphised DBW, and pollen and spores. This could be related to the proximity of emerged lands or islands and the relative shallowness of the sea (Carmeille et al., 2018).

The Tubiegatan section can be subdivided into four palynofacies intervals, from base to top (**Fig. 8**):

-Interval I (8.4 to 27 m) is characterized by elevated proportions of small size translucent phytoclast fragments, generally > 50%, low proportions of AOM and a small fraction of opaque phytoclasts. Pollen and spores, dinoflagellate cysts and foraminiferal linings occur in traces. Interval I coincides with the top of the sequence Tu1 and the sequence Tu2 (**Fig. 8**). The large proportions of translucent phytoclasts such as cuticles and the local influx of wood fragments (opaque phytoclasts) indicate the proximity of emerged lands.

-Interval II (27 to 33.9 m) presents high proportions of AOM (> 90%), and minor proportions of translucent phytoclasts. Amorphized DBW, opaque phytoclasts, DSOM, WPWF, pollen and spores, dinoflagellate cysts and foraminiferal linings occur in traces. This interval corresponds to the basal part of the Khodjaipak Fm., which shows low to moderate amount of preserved OM (TOC ≤2%, TOC=0.86 % on average; **Fig. 8**).

-Interval III (33.9 to 39.6 m) shows alternatively predominant proportions (> 85%) of AOM and amorphized DBW and rectangular AOM flakes. Minor proportions of opaque phytoclasts occur between 38 and 38.8m. DSOM, WPWF, pollen and spores, dinoflagellate cysts and foraminiferal linings occur in traces. Interval III is associated with the upper part of the Khodjaipak Fm., which shows enhanced accumulation of OM (TOC up to 6%, TOC=1.8% on average; **Fig. 8**).

-Interval IV (39.6 to 41 m) shows a predominance of AOM, however with lower proportions than within Interval III (AOM=61-79.7%), and moderate proportions (11.4-16%) of translucent phytoclasts. Opaque phytoclasts, pollen and spores, dinoflagellate cysts and foraminiferal linings occur in traces. It should be highlighted that the palynomorphs are not well-preserved and it is somewhat difficult to identify dinoflagellate cysts properly, especially in sample 09-E16 at 40 m. Palynofacies results from this sample should thus be taken with caution. Interval IV corresponds to the Upper carbonate interval of the Tubiegatan section, which shows low accumulation of OM (TOC=0.2% on average; **Fig. 8**).

4.6. Stable isotope signals and C/N records

Figure 9 presents the vertical evolution of $\delta^{13}C_{carb}$, $\delta^{18}O_{carb}$, $\delta^{13}C_{org}$ and $\delta^{15}N_{tot}$. In the lower carbonate interval, the $\delta^{13}C_{carb}$ remains positive (4-4.5‰) and relatively stable up to a small negative excursion (amplitude 0.3‰) at 14 m followed by a positive excursion (amplitude 0.7‰) at 20 m. The top of the lower carbonate interval (20 to 30 m) and the base of the Khodjaipak Fm. (30 to 33 m) record a rapid and significant decrease of $\delta^{13}C_{carb}$ (amplitude of *ca.* 4‰) to reach values close to 0. Very negative and fluctuating $\delta^{13}C_{carb}$ values (avg. -2.3‰) characterize the remaining part of the Khodjaipak Fm. (33-40 m). An overall decrease occurs from 33 to 38 m to reach the most negative value (-10‰), which is recorded in an organic microbial boundstone (F1c; **Fig. 10**). The signal then increases up to the top of the Khodjaipak Fm. In the upper carbonate interval, the values progressively increase but remain below 1‰. Overall, black nodular mudstones and microbial boundstones have the most negative $\delta^{13}C_{carb}$ (respectively -4‰ and -0.7‰ on average; **Fig. 10**).

The $\delta^{18}O_{carb}$ signal records strong variations between 0 and 12 m (amplitude of *ca*. 4‰) then progressively increases up to the top of the lower carbonate interval, with a maximum value of 0.8‰. The following Khodjaipak Fm. is marked by oscillating $\delta^{18}O_{carb}$ values (avg. -3.4‰) combined with a stepwise decrease up to 38 m (min.: -12‰; **Figs 9 and 10**). The top of the Khodjaipak Fm. and the following upper carbonate interval are characterized by a slight $\delta^{18}O_{carb}$ increase (max: -1.4‰).

The $\delta^{13}C_{org}$ signal (**Fig. 9**) fluctuates slightly around -25‰ for most of the lower carbonate interval, except near the top of the Tu1 sequence (9.5 to 12 m), where the values rapidly decrease (-27.4‰) and increase to reach their maximum (-23.4‰). The signal drops from 24 to 34 m, recording its lowest value (-28.5‰) near the transition between the palynofacies intervals II and III. Then the signal slightly increases and fluctuates between -27 and -28‰ up to the top of the Khodjaipak Fm.

The $\delta^{15}N_{tot}$ values are relatively stable in the lower carbonate interval (avg. 2.7‰). The Khodjaipak Fm. shows overall lighter $\delta^{15}N_{tot}$ (avg. 1.7‰) with significant fluctuations, between -1.1 and 4.5‰. The lowest values are recorded within the two anoxic intervals (**Fig. 9**).

The C/N ratio (**Fig. S3**) fluctuates between 5.5 and 81.9 (avg. 14.7) along the lower carbonate interval. The variations increase in amplitude (8.6 to 187; avg. 39.2) in the Khodjaipak Fm.

4.7. Major and trace elements

Most of major elements (Si, Fe, K, Ti) and many trace elements (Cr, Co, Th, Pb) show strong correlation ($R > 0.9$) with Al and are thus associated with the detrital fraction. Only few elements (Cd, Mo, Ni, U, V, Zn) are not ($R < 0.5$) or only slightly to moderately ($R < 0.9$) correlated with Al and show noticeable positive values of fraction in excess. This is particularly true for Mo, U and to a lesser extent V, which are particularly sensitive to oxygen variations. An increase of their concentrations compared with the upper continental crust values (1.5 ppm for Mo, 107 ppm for V and 2.8 ppm for U; McLennan, 2001) point to O_2-depleted conditions (Tribovillard et al., 2006; Lézin et al., 2013). Here, only the evolution of Mo_{xs} will be shown and discussed, U and V having the same evolution (**Fig. 11**). In the Khodjaipak Fm., punctual peaks of Mo_{xs} are observed, one at 34.5 m (73.2 ppm) and two others are observed at 37.2 and 38.3 m (with values up to 75.3 ppm; **Fig. 11**). In the second interval, the highest values of Mo_{xs} are related to the microbial boundstone (F1c).

To better constrain the O_2 variations, U/Th and V/Cr ratios were calculated. They are both used as oxygenation tracers at the water-sediment interface or in the sediment. Based on threshold values, defined by Jones and Manning (1994), these ratios allow to distinguish oxic ($U/Th < 0.75$ and $V/Cr < 2.00$), dysoxic and anoxic ($U/Th > 1.25$ and $V/Cr > 4.25$) conditions. In the Khodjaipak Fm., the values of ratios range from 0.95 to 8.00 for U/Th and from 1.40 to 13.40 for V/Cr (**Fig. 11**), indicating O_2-depleted conditions. Two intervals are characterized by high values of these ratios attesting for anoxic conditions: the AI1 (for Anoxic Interval n°1) extends from 33.4 to 35.0 m, the AI2 from 37.0 to 38.7 m (**Fig. 11**). The two anoxic intervals coincide with most of the elevated TOC values. The lower values below AI1, between AI1 and AI2 and above AI2 reflect dysoxic conditions.

5. DISCUSSION

5.1. Signal preservation and signification

5.1.1. Organic matter

The T_{max} from Rock-Eval analyses indicate the influence of a burial diagenesis consistent with the oil window (**Fig. 7**). The HI and OI values plotted in the Van Krevelen diagram (**Fig. S2**) suggest the presence of altered OM (Type IV) and/or continental (Type III) OM. Nevertheless, in the case of thermal diagenesis associated with marked burial of the sediments, the hydrogen bonds of organic molecules are particularly affected, leading to a decrease of the original HI values (Espitalié et al., 1985). HI values were thus originally higher than recorded, probably mostly fitting with a Type II (marine) OM, as reflected by predominant AOM in palynofacies. Furthermore, the local presence of orange-colored AOM, combined with a relatively low amount of pyrite (< 2%) could reflect an early diagenetic sulfurization of OM (Tribovillard et al., 2004). This process is widespread in anoxic marine environment and implies reactions between dissolved sulfide species and energy-rich moieties in the OM (e.g., alcohols, aldehydes). Sulfurized polymers (mostly lipids) are more resistant to microbial and/or thermal degradation (Raven et al., 2019), which could explain the preservation of substantial amounts of OM in the Khodjaipak Fm. The low OI values (**Fig. S2**) also suggest that most of the OM of the Khodjaipak Fm. is a thermally degraded Type II OM (Espitalié et al., 1985; Tyson, 1995). Accordingly, the measured TOC values are lower than the original ones. As TOC values reach up to ~6% in the Khodjaipak Fm., this implies high to very high original OM accumulation for a marine depositional environment. Despite a significant burial, the consistency of palynofacies, organic carbon geochemistry and sedimentary facies indicates that the OM retains part of the paleoenvironmental signal.

5.1.2. Clay minerals

The presence of kaolinite is compatible with limited burial temperatures, probably less than 160°C (Sucha et al., 1993). Dellisanti et al. (2010) estimated that for T_{max} ranging from 434 to 465°C, the content of illite in the IS-R1 should vary between 60 and 85%. In this context the illitization of potential former smectites or smectite-rich interstratified clay mineral such as IS-R0 may have occurred, these transformations taking place around 80-100°C, i.e. from 2 to 3 km of burial for a normal geothermal

gradient (Chamley, 1989). Both clay mineral assemblages and the maturity of the OM agree therefore with a minimal burial depth of *ca.* 2-3 km for the Khodjaipak Fm., if we consider a normal geothermal gradient. Occurence of initial smectite-rich clay minerals in the initial sediment is therefore a possibility and could correspond to current IS-R1. Preservation of kaolinite less sensitive to burial diagenesis allows to use these detrital clay minerals for palaeoclimate reconstruction, as no evidence of clay mineral authigenesis was recognized.

5.1.3. Carbonates

The petrographic examination of the lower carbonate interval and of the Khodjaipak Fm. deposits points to moderate chemical and/or mineralogical diagenetic transformations. The predominantly micritic facies of the lower carbonate interval show very small quantities of carbonate cements, except for late fracturation (e.g., **Fig. 4B**). The Khodjaipak Fm. is also cross-cut by late fractures infilled with fibrous gypsum, possibly formed through precipitation of sulfate-rich fluids coming from the overlying sabkha gypsum (Irgayli Fm.; **Fig. 3**). Microbial facies are predominantly micritic to microsparitic (**Fig. 6**). This probably indicates a moderate cementation and recrystallization of the carbonate minerals. The negative $\delta^{18}O_{carb}$ values comprised between 1‰ to -5‰ with two values reaching -8‰ and -12‰ (**Figs 9, 10**) indicate a potential contribution of meteoric water. However, in modern microbialites, the micrite to microspar transition can take place in the depositional environment. It is not necessarily related to meteoric cementation, but can also result from physico-chemical precipitation in alkaline water close to the microbialite surface, though the resulting isotopic values are generally not very negative (Dupraz et al., 2004, 2013). By contrast, the upper carbonate interval shows an intense cementation and a poor preservation of the facies, which indicates a probable strong diagenetic influence.

The effects of recrystallization by fluids circulation could affect the isotopic signal, particularly the $\delta^{18}O_{carb}$ primary signal, which is more sensitive than the $\delta^{13}C_{carb}$ (Immenhauser et al., 2002; Louis-Schmid et al., 2007). A strong covariation of $\delta^{13}C_{carb}$ and $\delta^{18}O_{carb}$ usually indicates the influence of meteoric fluids (e.g., Marshall, 1992). **Figure 10** presents a $\delta^{13}C_{carb}$ vs. $\delta^{18}O_{carb}$ cross plot. The linear least square regressions were calculated for the lower carbonate interval ($R^2 = 0.3$, P-value < 0.05) and

the Khodjaipak Fm. (R^2 = 0.3, P-value < 0.05). The results confirm a possible significant diagenetic imprint on the $\delta^{18}O_{carb}$, which is consequently not used for palaeoclimate reconstructions.

5.1.4. Sulfides and iron oxides

Given their morphology and their association with OM-clay complexes, the very small sulfur-rich globules (< 1µm in diameter) that are observed in microbial boundstones (**Fig. 6D**) are likely of microbial origin. They are very similar to the globules produced by sulfide-oxidizing anoxygenic phototrophic bacteria in modern hypersaline microbial mats (e.g., Pace et al., 2018). The Khodjaipak Fm. also shows moderate amounts of pyrite (< 1.5% of the bulk sediment) decreasing upward (**Fig. 3**). Pyrite is a common byproduct of microbial sulfate reduction and is common in organic-rich sedimentary formations (e.g., Rickard et al., 2017; Raven et al., 2019). The relatively low proportions of pyrite characterized here could be the result of the competition between reactive sulfides and OM for reactive Fe shortly after deposition (Shawar et al., 2018). A significant OM production, as postulated for the Khodjaipak Fm., could constitute a Fe sink and prevent pyrite precipitation (see section 5.3.3). At the micro-scale, the Fe oxides locally associated with OM (**Fig. 6F**) could derive from the oxidation of pyrite originally associated to OM-clay complexes. Fibrous gypsum filling fractures testifies of the post-depositional circulation of sulfate-rich fluids in the rock. These oxidizing fluids, probably coming from the overlying gypsum deposits (Irgayli Fm.; **Fig. 2**), could have induced the oxidation of primary pyrite. Overall, the top of the Khodjaipak Fm. is more affected by the circulation of oxidizing, probably saline fluids than its base.

5.2. Age of the Khodjaipak Fm. and stratigraphic relationship with the SW Gissar carbonate platform

Based on ammonite biostratigraphy, Abdullaev (2004) dated the Khodjaipak Fm. as Late Oxfordian to Kimmeridgian, while Mitta and Besnosov (2007) suggested a Late Oxfordian to Early Kimmeridgian age. The ammonite fauna identified in this study indicates a Middle Oxfordian age at least in Tubiegatan (**Fig. 3**). *Dichotomosphinctes luciaeformis* indicates an older age for the top of the lower carbonate interval (Transversarium Zone, Luciaeformis subzone), while *Subdiscosphinctes (Subdiscophinctes)* cf.

526 *richei* De Riaz */mindowe* Siemiradzki gives a more recent age (Transversarium zone, Schilli subzone)
527 in the upper part of the Khodjaipak Fm. The fact that all these deposits belong to two successive
528 subzones also indicates that there is no major stratigraphic hiatus associated with the hardground at the
529 top of the lower carbonate interval (**Fig. 3**).

530 A vast carbonate platform developed over the SW Gissar between the Early Callovian and potentially
531 the Kimmeridgian (Abdullaev, 2004; Nugmanov, 2010; Carmeille et al., 2018). Carmeille et al. (2018)
532 subdivided the platform succession in two major sequences: (i) a ramp developed during the Callovian
533 Sequence (CS; equivalent to the Lower Kugitang Fm. of Nugmanov, 2010), which is dated as Early-
534 Middle Callovian with ammonites, and possibly includes Upper Callovian deposits; (ii) The Upper
535 Jurassic Sequence (UJS; equivalent to the Upper Kugitang Fm. of Nugmanov, 2010) develops above a
536 major sequence boundary (SB2) and after a hiatus potentially encompassing the top of the Callovian
537 and the base of the Oxfordian (**Fig. 2**). In the SW Gissar, the UJS is dominated by mud or oncoid-rich
538 lagoonal deposits (the Gardarin Fm. of Abdullaev et al., 2010) passing southward to ooid shoal
539 grainstones and peri-reefal facies. Carmeille et al. (2018) proposed a correlation between several $\delta^{13}C_{carb}$
540 excursions recorded in the UJS and the well-dated NW Tethyan bivalve $\delta^{13}C$ record compiled by Dera
541 et al. (2011). This correlation would date the UJS as Early to Late Oxfordian. The stratigraphic
542 relationships between the SW Gissar carbonate platform and the Khodjaipak Fm. are key to understand
543 the palaeogeographic setting and to establish a depositional model for the organic carbonates.

544 Some authors (e.g., Abdullaev, 2004; Nugmanov, 2010) propose a model where organic shales
545 (Khodjaipak Fm.) accumulate in a starved basin separated from the lagoon (Gardarin Fm.) by a large-
546 scale barrier reef (Urtabulak Fm.). Besides the presence of Oxfordian ammonite specimens recognized
547 in the Khodjaipak Fm., the lower carbonate interval of the Tubiegatan section shows heavy $\delta^{13}C_{carb}$
548 values (4.25‰ on average), which largely overlap with the values measured in the UJS lagoonal deposits
549 (4.00‰ on average; **Fig. 10**). Consequently, the lower carbonate interval, underlying the Khodjaipak
550 Fm. could be time equivalent of part of the UJS inner shelf deposits in the SW Gissar.

551 The UJS is subdivided into two medium-scale sequences, UJS1 and UJS2, which are separated by a
552 major sequence boundary which resulted in the exposure of the northern part of the SW Gissar platform

(SB3; **Fig. 12**; Carmeille et al., 2018). We propose two correlation hypotheses between the organic-rich Tubiegatan succession and the SW Gissar inner platform deposits, based on the carbon-isotope signal and the sequence stratigraphy.

5.2.1. Hypothesis n°1

The first hypothesis (**Fig. 12A**) correlates the $\delta^{13}C_{carb}$ positive peak (*ca.* 0.5-1.2‰) recorded in the middle part of UJS1 in the Baglydara and Pyandzh Ob sections with a similar excursion in the lower carbonate interval of the Tubiegatan section (*ca.* 0.5‰ of amplitude, **Fig. 12A**). Above, a gradual decrease of $\delta^{13}C_{carb}$ is recorded up to SB3, leading to a marked negative excursion in the $\delta^{13}C_{carb}$ (amplitude > 0.5‰ in Baglydara, > 2‰ in Pyandzh Ob and *ca.* 1‰ in Derbent; **Fig. 12A**). The $\delta^{13}C_{carb}$ then progressively increases of 1.5 to 2‰ above SB3. In Tubiegatan, the $\delta^{13}C_{carb}$ shows a decrease of *ca.* 4‰ encompassing the top of the lower carbonate interval and the basis of the Khodjaipak Fm. Then, the values drop down to -10‰ in Khodjaipak Fm. before a progressive increase (amplitude > 10‰) from the top of the Khodjaipak Fm. to the upper carbonate interval. Hypothesis n°1 implies a correlation of these two negative peaks of different amplitude. In this scenario, the Khodjaipak Fm. would have deposited at a period of low sedimentation rate (recorded by burrowed horizons) and partial subaerial exposure of the platform associated with SB3 (Carmeille et al., 2018).

5.2.2. Hypothesis n°2

In the second hypothesis, we correlate the slight positive excursion recorded in Tubiegatan with three similar excursions (amplitude of *ca.* 1‰) recorded in the first half of UJS2 in the SW Gissar sections (blue colour, **Fig. 12B**). This is followed by rapid 1 to 1.5‰ fluctuations in the $\delta^{13}C_{carb}$ in Baglydara or by 1 to 2‰ negative carbon-isotope excursions in Pyandzh Ob and Derbent, about 40–60 m under the nodular gypsum strata of the SW Gissar platform (**Fig. 12B**). The same negative excursion was recorded below evaporites in other SW Gissar sections (e.g., Langar; Carmeille et al., 2018). In Derbent, the top of the carbonate succession shows a *ca.* 2‰ positive excursion in the $\delta^{13}C_{carb}$ record. This excursion can be correlated with the positive excursion recorded at the top of the Khodjaipak section. Hypothesis n°2 is supported by sedimentological arguments. UJS2 displays several bioturbated horizons (e.g., in Baglydara and Derbent sections). Similar burrowed limestones are also observed along the lower

carbonate interval in Tubiegatan, at Tu1 and Tu2 sequence boundaries (**Figs 3, 12**). In the proposed correlation, the burrowed horizons would be approximately in the same stratigraphic interval as in Tubiegatan. Inner platform stromatolites and pellet-rich deposits form the transition between the organic carbonates (Khodjaipak Fm.) and the overlying nodular gypsum. Similarly, UJS2 is overlain by sabkha gypsum over the whole SW Gissar (**Fig. 12**), which reflects a progressive restriction and an increasing salinity on the platform (Carmeille et al., 2018). In this scenario, the organic carbonates would form contemporaneously of an evaporative, low energy carbonate lagoon rich in gypsum pseudomorphs (**Fig. 12**). This second hypothesis appears to be the most likely scenario, and will be used throughout the paper.

5.3. Sedimentological and geomicrobiological models for the Khodjaipak organic carbonates

5.3.1. Depositional environment of the organic carbonates

The fine-grained textures, conjugated with abundant and thin microbial laminations (**Figs 3 and 5**), suggest a low-energy depositional environment for the Khodjaipak organic sediments (Droste, 1990; Warren, 2011). The intercalation of thin shell beds (**Figs 3 and 4F**) indicates the punctual influence of hydrodynamic events, probably storms, in this predominantly quiet environment. The presence of early diagenetic sulfate pseudomorphs (**Fig. 5B**) may also indicate punctual hypersaline conditions within the sediment (Warren, 2011). The Khodjaipak Fm. organic carbonates are overlain by intertidal to shallow subtidal lagoon carbonates and then by supratidal sabkha chicken-wire gypsum (**Figs 1C and 3**). Similar successions have been documented in the shallow subtidal to supratidal sequences of the Holocene Abu Dhabi sabkha (e.g., Lokier and Steuber, 2008; Aref and Taj, 2018), but also in the Upper Jurassic to Lowest Cretaceous Purbeck beds (northern France-southern UK; e.g., Shearman, 1966; West, 1975; Schnyder et al., 2009) or in the Upper Permian of the Dolomites (Italy; e.g., Hardie, 1986). Jahnert and Collins (2012) and Bouton et al. (2016) have also shown that thin storm shell beds can be trapped and preserved within shallow water (< 1 m deep) hypersaline lagoon microbialites from Australia (Shark Bay) and Cuba (Cayo Coco). In the absence of subaerial exposure evidence, we postulate that the Khodjaipak Fm. was deposited in a shallow subtidal environment (**Fig. 13A**). This would imply that

607 part of the pelagic fauna (e.g., ammonites; **Figs 4 and 5**) could have undergone a post-mortem drift
608 (e.g., Olivero and Raffi, 2018). The documented benthic foraminifera (e.g., *Lenticulina* and
609 *Reinholdella*) are opportunistic, well adapted to low oxygen levels and can live in shallow water (Rita
610 et al., 2016). A shallow environment (depth of *ca.* 30 m) was hypothesized for the deposition of the
611 organic-rich part of the Middle-Upper Oxfordian Hanifa Fm. on the Arabian Platform (Warren, 2011).
612 Relatively shallow seas and the proximity of emerged lands or islands during the Khodjaipak Fm.
613 deposition are also consistent with the common occurrence of terrestrial-derived materials in
614 palynofacies, such as opaque and translucent phytoclasts, DSOM, WPWF, amorphized DBW, and
615 pollen and spores.

616 The highest TOC values are found in nodule-rich carbonate facies (F1b; **Fig. S1**). On the opposite,
617 quartz-rich siltstones have relatively low TOC, which indicates that carbonate production is associated
618 with OM concentration, while detrital influx probably favored OM dilution. Palynofacies yielding
619 opaque and translucent phytoclasts between 38 and 41 m (**Fig. 8**) indicate an increase of terrestrial
620 organic inputs at the top of the Khodjaipak Fm. (**Fig. 13A**). This interval rich in terrestrial phytoclasts
621 occurs after the decline in kaolinite proportion (**Fig. 3**) and precedes sabkha gypsum deposition. During
622 the Middle-Late Jurassic, periods marked by drastic changes in kaolinite are often interpreted as
623 variations in humidity conditions: high proportions in kaolinite point to humid conditions and low
624 kaolinite proportions to a drier climate (Pellenard and Deconinck, 2006; Schnyder et al., 2006; Brigaud
625 et al., 2014; Pellenard et al., 2014). Part of the opaque phytoclasts could also derive from wildfires in
626 the nearby continental areas. All these observations indicate that a climate aridification occurred during
627 the deposition of the Khodjaipak Fm. and could have culminated with the platform-wide development
628 of sabkha (Irgayli Fm.; **Figs 2, 12 and 13A**; Carmeille et al., 2018).

629 ### 5.3.2. Geomicrobiological model

630 The thinly laminated microfabrics (**Fig. 5**), the presence of peloids and intra-carbonate OM (**Figs 5C**
631 **and 5E**), the potential preservation of EPS remnants (**Fig. 6C**) and the abundance of AOM in
632 palynofacies (**Fig. 8**), all suggest that most of the OM was produced by microorganisms (bacteria,
633 archaea and/or unicellular algae), notably in benthic microbial mats. The preservation of microbial

lamination can be partly explained by the scarcity of bioturbation, which in turns reflects the low oxygenation of the bottom sediment (Warren, 2011). Trace elements concentrations and ratios indicate alternating anoxic and suboxic conditions (**Fig. 11**). The potential development of contemporaneous organic-poor carbonates in the SW Gissar (**Figs. 12 and 13A**) could indicate water stratification, where the Khodjaipak Fm. accumulated in poorly oxygenated bottom water. These O_2-depleted conditions promoted the preservation of OM -possibly through early sulfurization- and supported the development of anaerobic microorganisms in the mats (e.g., methanogenic and methanotrophic microbes; **Fig. 13B**). The two anoxic episodes are associated with the highest TOC, but also with the lowest $\delta^{13}C_{carb}$ and $\delta^{15}N_{tot}$ (**Fig. 9**). During these episodes, we suggest that extensive denitrification decreased nitrate availability and therefore, phytoplankton (including cyanobacteria) capable of using an alternate source of nitrogen such as N_2 may have become quantitatively important, leading to a $\delta^{15}N_{tot}$ values close to zero (**Fig. 9**; Quan and Falkowski, 2009). In addition, the dinitrogen gas increase could be a consequence of the anammox bacterial activity, which converts ammonium from the anoxic water to N_2 by anaerobic metabolic reaction (**Fig. 13B**; Kuypers et al., 2003; Kuenen, 2008).

In shallow hypersaline lagoons, the majority of OM derives from photosynthesis (Warren, 2011). However, there is only indirect evidence for the presence of photoautotrophic microorganisms in the Khodjaipak Fm. Sulfur-rich globules in OM-clay complexes (**Fig. 6D**) could indicate the activity of anoxygenic phototrophs such as purple sulfur bacteria (Pace et al., 2018). Whether oxygenic photosynthesis occurred in the Khodjaipak Fm. remains uncertain. The micritic and microsparitic peloids observed in microbial boundstones (F1c; **Figs 5C and 6A to 6D**) are typically related to microbial degradation of EPS. In modern mats, the degradation of some EPS components by heterotrophic bacteria, e.g., sulfate-reducing bacteria (SRB), leads to the formation of carbonate peloids by increasing alkalinity and releasing cations adsorbed by EPS such as calcium (e.g., Dupraz et al., 2004; Visscher and Stolz, 2005; Pace et al., 2018). The presence of sulfate pseudomorphs in the Khodjaipak Fm. (**Fig. 5B**) indicates that porewaters were sulfate-rich. Sulfates could have been reduced by SRB to (hydrogen) sulfides (**Fig. 13B)** and part of the sulfides could have been subsequently precipitated as pyrite or bound to part of the EPS through OM sulfurization. The study conducted by

Arp et al. (2008) in the Upper Jurassic of north Germany documents calcitized pseudomorphs of gypsum with very low $\delta^{13}C_{carb}$ within stromatolites, suggesting oxygen-depleted sulfate-bearing environments associated with high rates of methane production. These authors made the hypothesis that the gypsum was replaced by magnesian calcite at the transition of suboxic and sulfidic zones within the mats during sulfate-driven anaerobic oxidation of methane (SD-AOM; Reeburgh, 2007; Himmler et al., 2018). The $\delta^{13}C_{carb}$ values measured in the Khodjaipak Fm. (ranging from -10‰ to +2‰) are not negative enough to support this process, but fit well with the $\delta^{13}C_{carb}$ range of hypersaline lake microbial mats with a high organic productivity and SRB activity (Vasconcelos et al., 2006; Glunk et al., 2011; Dupraz et al., 2013). Both geochemical and petrographic data suggest a strong contribution of microbial sulfate reduction to carbonate precipitation. However, SD-AOM cannot be totally ruled out. Indeed, a late recrystallization of carbonates in e.g., meteoric water, or a contribution of bioclast dissolution could have led to an increase of the original $\delta^{13}C_{carb}$ values (e.g., De Boever et al., 2009).

5.3.3. Regional depositional model

On epeiric platforms, OM accumulates in two types of mesohaline settings, often in association with evaporites (Warren, 2011): (i) intrashelf basins or (ii) shelf edge depressions. Both cases imply a tectonically and/or climatically-driven restriction of shelf water and the formation of a hydrographic barrier partially isolating a water body, leading to the formation of stratified brines. In the Oxfordian Hanifa Fm., reef or bioclastic platform rims built during transgressions, and subsequently isolated the intrashelf basins during sea level falls (Carrigan et al., 1995; Warren, 2011). The Late Jurassic semi-arid climate also enhanced the formation of anoxic/dysoxic saline brines in coastal lagoons and lakes from the Purbeck Beds of Dorset (UK, Late Tithonian-Berriasian). Combined with freshwater inputs linked to a climatic change toward slightly more humid conditions during the Berriasian, this ultimately led to the development of water stratification and the deposition of OM-rich facies linked to enhanced primary productivity in surface waters and its preservation in anoxic bottom water brines (Schnyder et al., 2009). Similar examples of coastal marine sediment enriched in OM are known from Holocene coastal salinas and hypersaline lagoons of Australia (Bauld, 1981; McKirdy et al., 1992; Coshell and Rosen, 1994).

The Kugitang cliffs, located *ca.* 10 km south of Baglydara and 35 km east of Tubiegatan, display the largest reefs outcropping in the SW Gissar (up to 80 m high; Ilyn and Fortunatova, 1988). These reefs could be a stratigraphic equivalent of UJS1, where peri-reefal bioclastic deposits were documented (**Fig. 13A**; Carmeille et al., 2018). Such reefs complexes could have formed a hydrographic barrier limiting water exchanges between the oxygenated inner platform water and the stratified brines in Tubiegatan. Based on the correlation hypotheses proposed **Figure 12**, we built a four steps carbonate shelf to anoxic intrashelf lagoon evolution scenario which shares some similarities -but is not strictly equivalent- with that of the Purbeck Beds of Dorset or that of the above-mentioned Holocene Australian coastal lakes and lagoons (**Fig. 13A**):

-*step 1*: the facies of the lower carbonate interval (sequences Tu1, Tu2 and the basis of Tu3) show evidence for a good oxygenation of the water column. At that time, it is unknown whether Tubiegatan was located on a seaward opened mid to outer shelf or within a well oxygenated, non-stratified lagoon. At the top of the lower carbonate interval (Tu3 transgressive cycle, Luciaeformis SZ, Transversarium Zone, Middle Oxfordian, **Fig. 3**), a flooding associated with a low sedimentation rate could explain the formation of a subaqueous hardground. Reworking and erosion of coastal vegetalized areas due to the transgression led to local inputs of wood debris, as indicated by opaque phytoclasts occurences in the palynofacies (**Fig. 8**). An intrashelf lagoon could have formed following the development of two hydrographic barriers: (i) eastward, large coral reefs located to the south of the SW Gissar; (ii) a hypothetical second hydrographic barrier located westward and/or southward (not outcropping).

-*step 2*: the presence of detrital kaolinite, usually formed during pedogenesis in intertropical climate, suggests enhanced water precipitation at the beginning of the Khodjaipak Fm. deposition (Luciaeformis to Schilli SZ, Transversarium Zone, Middle Oxfordian). Freshwater inputs, combined with limited lagoon to basin water exchange leads to progressive water stratification. Extensive microbial mats developed in the suboxic brines at the bottom of the intrashelf basin. Developing benthic and possibly planktonic algal/bacterial productivity led to a relative increase in OM deposition (TOC ≤ 2%), with palynofacies dominated by AOM. Shell beds may have derived from the reworking of peri-reefal sediments by storm currents leading to possible punctual re-oxygenation of the bottom water mass.

-*step 3*: a regional aridification is attested by the disappearance of kaolinite and increase of IS-R1 possibly through illitization of original smectite, and characteristic of semi-arid climate and possible wildfires as indicated by opaque wood fragments input. The associated sea level drop led to the exposure of the reef complex and to an increasing isolation of the intrashelf basin, which became near permanently anoxic (**Fig. 13A**; Schilli Subzone, Transversarium Zone, Middle Oxfordian). Step 3 is also the period of maximum microbial mat development. The climatic conditions might still allow some periodic freshwater inputs supporting primary productivity in surface waters and the local development of ligneous aquatic or emerged coastal plants producing AOM and DBW, respectively (**Fig. 8**). The shallow, restricted water may have promoted in situ amorphization/gelification processes of the DBW. As a result of enhanced organic productivity (possibly from organic various sources) and developing stratification, anoxia and OM deposition reached a maximum (TOC up to 6%).

-*step 4*: the increasing evaporation progressively decreasing water depth and lowering freshwater input, could have limited water stratification. The resulting mixing of surface and bottom water led to the oxygenation of the bottom of the intrashelf basin and to OM oxidation (TOC ≤ 1%; **Fig. 8**). Intertidal to shallow subtidal lagoon deposits, including stromatolites, prograded and progressively filled the accommodation space (Schilli to post-Schilli Subzones, Middle Oxfordian). Finally the nodular gypsum accumulation records the development of a large scale sabkha covering the whole SW Gissar region (**Fig. 3**). These sabkha deposits are either anterior to- or partly contemporaneous with the thick salt-anhydrite series of the Gaurdak Fm. (Kirshin, 2007; Abdullaev et al., 2010; Carmeille et al., 2018). At this time, regional subsidence is very low (Brunet et al., 2017). Compression and uplifts in the Afghan and Central Iranian blocks related to the closure of the Waras-Panjaw Ocean (Central Afghanistan) probably leads to the restriction of the ADB and to the deposition of the Gaurdak salt (Barrier et al., 2018). Overall, the organic-rich deposits of Khodjaipak Fm. may record the onset of the isolation of the ADB from more open areas (e.g., the South Caspian Basin). In this case the new datings provided by ammonites identification at Tubiegatan would demonstrate that this disconnection would have begun at the end of the Middle Oxfordian. This tectonic disconnection, combined with a regional aridification

could have led to the progressive increase of evaporation and subsequent organic-rich deposits in intrashelf depressions on the carbonate platform.

5.4. Context and origin of worldwide-scale organic-rich accumulations during the Oxfordian-Kimmeridgian

The Early Oxfordian-Early Kimmeridgian period is characterized by the multiplication of organic-rich deposits worldwide and could be considered as a Late Jurassic Ocean Anoxic Event as proposed by Trabucho-Alexandre et al. (2012) and Martinez & Dera (2015). Major source rocks developed during this period, e.g., the Hanifa Fm., the Kimmeridge Clay Fm., the Smackover Fm. (Warren, 2011). **Figure 14** compiles the facies and composition of these organic-rich formations. On the Arabian Platform, the Lower to Upper Oxfordian organic-rich Hanifa Fm. accumulated in small and semi-isolated intrashelf basins, where seawater was stratified and OM accumulated in dysoxic to anoxic bottom water (Droste, 1990; Carrigan et al., 1995; Vahrenkamp et al., 2015). The progressive isolation of these basins could be the consequence of an uplift of the Eastern margin of the Arabian Plate. The restriction of the intrashelf basins subsequently led to the evolution from normal marine shallow-water carbonates during the Kimmeridgian (Jubaila Fm.) to restricted-marine and evaporitic deposits during the Tithonian (Arab A, B, C and Hith Fms). In Wadi Nisah (Saudi Arabia), the Hanifa Fm. is composed of fine-grained carbonates and biosiliceous facies (Hawtah Member) overlain by organic-rich silty carbonates alternating with burrowed skeletal facies (Ulayyah Member; Eltom et al., 2017). These deposits are interpreted to reflect the circulation of nutrient-rich currents derived from shelf edge upwellings into the intrashelf basins (Eltom et al., 2017). The basal sequence C of the Smackover Fm. and its distal equivalent, the Haynesville Shales, are major source rocks in the United States Gulf Coast. These formations include organic-rich (up to 6% TOC) and biosiliceous lime mudstones, which accumulated in anoxic intrashelf basins delimited by carbonate platforms and islands (Heydari et al., 1997; Hammes et al., 2011; **Fig. 14**). Some of these facies could be of microbial origin (Hammes et al., 2011). In the Neuquen Basin (Argentina), the unit 1 of La Manga Fm. consists of basinal organic rich shale-limestone sequences (up to 4.5% TOC), which are locally rich in radiolarians (Palma et al., 2014). These deposits could have accumulated in half grabens, close to the hanging wall of normal faults, while shallow water

carbonates could have been produced on the foot wall. They are overlain by Middle-Upper Oxfordian intertidal stromatolites with fenestrae and mud-cracks (Palma et al., 2015; **Fig. 14**) and finally by sabkha deposits of the Auquilco Fm., recording an overall shallowing trend. A common stratigraphic pattern characterizes these Middle to Upper Oxfordian organic-rich formations: (i) subtidal normal marine carbonates are overlain by (ii) mesohaline organic facies (often microbial). This succession reflects the progressive stratification of the water, sometimes associated with- or followed by an increase of the salinity. Then, (iii) intertidal to shallow subtidal carbonates are overlain by (iv) sabkha deposits, indicating the filling of the accommodation space and a further increase of salinity. The quasi-contemporaneous formation of intrashelf basins on the northern and southern margins of the Tethys, in the Gulf of Mexico and on the eastern margin of the Pacific during the Middle to Late Oxfordian could reflect the early stages of the large-scale compressive tectonic events known as Late Cimmerian or Neo Cimmerian in western central Asia (Late Jurassic to Early Cretaceous; i.e. Boulin, 1990) leading to margin inversions.

The influence of these multiple organic accumulations on the global carbon cycle can be questioned. In the subalpine basin, a short-term negative $\delta^{13}C_{carb}$ excursion (*ca.* 0.5-2‰) in the Transversarium Zone punctuates a long-term positive trend encompassing the Plicatilis–Transversarium interval (Padden et al., 2001; Louis-Schmid et al., 2007; Rais et al., 2007). A negative excursion was also measured in nodular micritic limestones known as Knollenkalk in the Swiss Jura Mountains (Rais et al., 2007; **Fig. 14**). These excursions could be the result of gas hydrate dissociation (Jenkyns, 2003). The compilation of western Tethyan belemnite $\delta^{13}C$ by Martinez and Dera (2015) shows a major negative carbon isotope excursion (amplitude of *ca.* 4‰) at the Middle to Late Oxfordian transition (Transversarium-Bifurcatus Zone; **Fig. 14**). This period coincides with a maximum in the high eccentricity of the 9 Myr orbital cycle as defined by Martinez & Dera (2015). According to these authors the maxima of eccentricity leading to altered climatic conditions. Stratification of the water and anoxia develop preferentially during seasonal humid phases, inducing terrestrial runoff and nutrient inputs. During arid phases, increasing evaporation leads to homogenization of the water mass (Martinez and Dera, 2015). The sedimentological, geochemical and mineralogical evolution of the Khodjaipak Fm. (**Fig. 13A-B**) fits

795 well with this scenario. In addition, the CO_2 outgassing from protracted magmatic activity along
796 spreading ridges and subduction zones could have induced warming climate during the Late Jurassic,
797 leading to increase the flux of nutrients and, as a consequence, the biological productivity (e.g., Jones
798 and Jenkyns, 2001; Georgiev et al., 2017). However, no lines of evidence of this long-lived volcanic
799 activity were still published. Overall, the multiplication of OM storage events during the top of the
800 Middle Oxfordian and the base of the Upper Oxfordian (**Fig. 14**) could have resulted from the
801 conjunction of (i) an orbital-driven, changing seasonal climate coupled to (ii) an increase in continental
802 and/or oceanic nutrient inputs and (iii) the initiation of tectonic inversion on several margins.

803 ## CONCLUSION

804 The Khodjaipak Fm. is composed of organic-rich carbonates, marls and siltstones which were deposited
805 on a vast part of the Amu Darya Basin. These deposits were newly dated to the Middle Oxfordian,
806 Transversarium Zone (Luciaeformis and Schilli Subzones). The predominant facies are organic
807 laminated siltstones, nodular mudstones reaching ~6% of total organic carbon, and thinly laminated
808 microbial boundstones. These organic-rich deposits are overlain by shallow water lagoon and sabkha
809 deposits. Palynofacies and petrographic analyses show that a significant proportion of the OM was
810 produced in benthic microbial mats together with possible secondary contributions of algal/bacterial
811 primary production in surface waters and local developments of aquatic macrophytes. Rock-Eval
812 pyrolysis analyses indicate that the OM is mature (reaching the oil window), and that a minimal burial
813 depth of 2-3 km was reached. The concentrations and ratios of trace metallic element record two anoxic
814 episodes punctuated by dysoxic periods. These anoxic episodes are associated with the highest total
815 organic carbon values, enhanced aquatic primary production (possibly from several sources as indicated
816 by palynofacies), $\delta^{15}N_{tot}$ close to zero and the most negative $\delta^{13}C_{carb}$ values. Both microfabrics and
817 palynofacies indicate a significant contribution of microbial communities to the formation of carbonates.
818 The presence of sulfate pseudomorphs, sulfur globules and pyrite could indicate bacterial sulfur cycling.
819 The light $\delta^{13}C_{carb}$ signature of stromatolites and carbonate nodules could be related to precipitation
820 influenced by sulfate reduction. Overall, the Khodjaipak Fm. is interpreted to have formed in a shallow
821 water stratified, probably slightly hypersaline (intrashelf?) basin, periodically isolated from the

contemporaneous lagoon by pre-existing carbonate platform reliefs (e.g., coral reefs). The Middle-Upper Oxfordian is characterized by the multiplication of comparable organic-rich deposits in the northern and southern Tethys, in the Central Atlantic and in the Pacific. Some of these deposits could also have formed in shallow water anoxic conditions, which contrasts with the basin anoxia model characterizing some Cretaceous OAE. Anoxic conditions may have been enhanced by the conjunction of a contrasted arid/humid climate and the tectonic inversion of several margins. The multiplication of such shallow water anoxic episodes could have led to major carbon cycle perturbations from the Middle Oxfordian till the Early Kimmeridgian.

ACKNOWLEDGEMENTS

This study was funded by Total S.A. The scientists of the Institute of Geology and Geophysics of Uzbek Academy of Sciences of Tashkent (Uzbekistan), especially Irina Sidorova and Dmitriy Mordvintsev, are acknowledged for their logistic support in the field. The authors express their gratitude to Grégoire Bex for its assistance in the field, Léa Pigot and Philippe Blanc for the preparation of the thin sections, and Anne-Lise Santoni, Théophile Coquerez and Ludovic Bruneau for their assistance with analyses.

Bibliography

Abdullaev, G.S., 2004. Biostratigraphy, lithofacies and oil and gas perspectives of the Amu-Darya northern margin Jurassic carbonates. Abstract of the thesis, Geology and Geophysics Institute, archives, Tashkent, 39 p. (in Russian).

Abdullaev, G.S., 1999. Detailing of Stratigraphy of Upper Jurassic Carbonate Complex of Western Uzbekistan - Basis for Increasing Effectiveness of Oil-Gas Exploration 33, 297–304.

Abdullaev, G.S., Mirkamalov, H.H., 2001. Stratigraphy of the Jurassic high-gamma activity rocks of the Bukhara-Khiva region and its importance for the modelisation of the carbonate formation. Collect. Tr. IGIRNIGM Tashkent 13–24.

Abdullaev, G.S., Mirkamalov, H.H., Evseeva, G.B., 2010. Oil and gas bearing reefal facies of the Jurassic carbonate unit of the Amu-Darya basin (southern and southwestern Uzbekistan) and their correlation with reef creation within the paleobasins of the Tethys. Theor. Pract. Asp. Oil Gas Geol. Cent. Asia Solut. Mod. Probl. Domain NGGI Tashkent 39–49.

Aref, M.A., Taj, R.J., 2018. Recent evaporite deposition associated with microbial mats, Al-Kharrar supratidal–intertidal sabkha, Rabigh area, Red Sea coastal plain of Saudi Arabia. Facies 64, 28. https://doi.org/10.1007/s10347-018-0539-y

Arp, G., Ostertag-Henning, C., Yücekent, S., Reitner, J., Thiel, V., 2008. Methane-related microbial gypsum calcitization in stromatolites of a marine evaporative setting (Münder Formation, Upper Jurassic, Hils Syncline, north Germany). Sedimentology 55, 1227–1251. https://doi.org/10.1111/j.1365-3091.2007.00944.x

Barrier, E., Vrielynck, B., Brouillet, J.-F., Brunet, M.-F., 2018. Paleotectonic Reconstruction of the Central Tethyan Realm. Tectono-Sedimentary-Palinspastic maps from Late Permian to Pliocene. CCGM/CGMW, Paris, http://www.ccgm.org. Atlas of 20 maps (scale: 1/15 000 000).

Bartolini, A., Baumgartner, P.O., Guex, J., 1999. Middle and Late Jurassic radiolarian palaeoecology versus carbon-isotope stratigraphy. Palaeogeogr. Palaeoclimatol. Palaeoecol. 145, 43–60. https://doi.org/10.1016/S0031-0182(98)00097-2

Baudin, F., Tribovillard, N., Laggoun-Défarge, F., Lichtfouse, E., Monod, O., Gardin, S., 1999. Depositional environment of a Kimmeridgian carbonate 'black band' (Akkuyu Formation, south-western Turkey). Sedimentology 46, 589–602. https://doi.org/10.1046/j.1365-3091.1999.00226.x

Baudin, F., Tribovillard, N., Trichet, J., 2007. Géologie de la matière organique. EDP sciences.

Bauld, J., 1981. Geobiological role of cyanobacterial mats in sedimentary environments: production and preservation of organic matter. BMR J. Aust. Geol. Geophys. 6, 307–317.

Behar, F., Beaumont, V., Penteado, H.L.D.B., 2001. Rock-Eval 6 Technology: Performances and Developments. Oil Gas Sci. Technol. 56, 111–134. https://doi.org/10.2516/ogst:2001013

Bernier, P., Enay, R., 1972. Figures d'émersion temporaire et indices de sédimentation a très faible profondeur dans le Portlandien et le Kimméridgien supérieur (Calcaires en plaquettes) du Grand-Colombier-de-Culoz (Ain, France). Bull. Société Géologique Fr. S7-XIV, 281–292. https://doi.org/10.2113/gssgfbull.S7-XIV.1-5.281

Besnosov, N.V., Mitta, V.V., 1995. Upper Jurassic Ammonitids and Black Shales of Central Asia. - Russ. Geol. Oil Inst. VNIGNI.

Boulin, J., 1990. Neocimmerian events in Central and Western Afghanistan. Tectonophysics 175, 285–315. https://doi.org/10.1016/0040-1951(90)90177-A

Bouton, A., Vennin, E., Pace, A., Bourillot, R., Dupraz, C., Thomazo, C., Brayard, A., Désaubliaux, G., Visscher, P.T., 2016. External controls on the distribution, fabrics and mineralization of modern microbial mats in a coastal hypersaline lagoon, Cayo Coco (Cuba). Sedimentology 63, 972–1016. https://doi.org/10.1111/sed.12246

Brigaud, B., Vincent, B., Carpentier, C., Robin, C., Guillocheau, F., Yven, B., Huret, E., 2014. Growth and demise of the Jurassic carbonate platform in the intracratonic Paris Basin (France): Interplay of climate change, eustasy and tectonics. Mar. Pet. Geol. 27, 853-894

Brumsack, H.-J., 2006. The trace metal content of recent organic carbon-rich sediments: Implications for Cretaceous black shale formation. Palaeogeogr. Palaeoclimatol. Palaeoecol. 232, 344–361. https://doi.org/10.1016/j.palaeo.2005.05.011

Brunet, M.-F., Ershov, A.V., Korotaev, M.V., Melikhov, V.N., Barrier, E., Mordvintsev, D.O., Sidorova, I.P., 2017. Late Palaeozoic and Mesozoic evolution of the Amu Darya Basin (Turkmenistan, Uzbekistan). Geol. Soc. Lond. Spec. Publ. 427, 89–144. https://doi.org/10.1144/SP427.18

Carignan, J., Hild, P., Désaubliaux, G., Morel, J., Yeghicheyan, D., 2001. Routine Analyses of Trace Elements in Geological Samples using Flow Injection and Low Pressure On-Line Liquid Chromatography Coupled to ICP-MS: A Study of Geochemical Reference Materials BR, DR-N, UB-N, AN-G and GH. Geostand. Newsl. 25, 187–198. https://doi.org/10.1111/j.1751-908X.2001.tb00595.x

Cariou, E., Hantzpergue, P., 1997. Groupe Français d'Etudes du Jurassique, Biostratigraphie du Jurassique Ouest-Européen et Méditerranéen. Zonations parallèles et distribution des invertébrés et microfossiles. Bulletin des Centres de Recherches et Exploration Production d'Elf-Aquitaine, v. 17, p. 400.

Carmeille, M., Bourillot, R., Brunet, M.-F., Pellenard, P., Fürsich, F.T., Schnyder, J., Barrier, E., Blanpied, C., Sidorova, I., 2018. Architecture and sedimentary evolution of the southwestern Gissar carbonate platform (Uzbekistan) during the Middle–Late Jurassic. Mar. Pet. Geol. 97, 437–465. https://doi.org/10.1016/j.marpetgeo.2018.07.021

Carpentier, C., Lathuilière, B., Ferry, S., Sausse, J., 2007. Sequence stratigraphy and tectonosedimentary history of the Upper Jurassic of the Eastern Paris Basin (Lower and Middle Oxfordian, northeastern France). Sedimentary Geology, 197(3-4), 235-266.

Carrigan, W.J., Cole, G.A., Colling, E.L., Jones, P.J., 1995. Geochemistry of the Upper Jurassic Tuwaiq Mountain and Hanifa Formation Petroleum Source Rocks of Eastern Saudi Arabia, in: Katz, B.J. (Ed.), Petroleum Source Rocks, Casebooks in Earth Sciences. Springer Berlin Heidelberg, Berlin, Heidelberg, pp. 67–87. https://doi.org/10.1007/978-3-642-78911-3_5

Catuneanu, O., Galloway, W.E., Kendall, C.G.S.C., Miall, A.D., Posamentier, H.W., Strasser, A., Tucker, M.E., 2011. Sequence Stratigraphy: Methodology and Nomenclature. Newsl. Stratigr. 44, 173–245. https://doi.org/10.1127/0078-0421/2011/0011

Chamley, H., 1989. Clay Formation Through Weathering, in: Clay Sedimentology. Springer, Berlin, Heidelberg, pp. 21–50. https://doi.org/10.1007/978-3-642-85916-8_2

Collin, P.Y., Kershaw, S., Tribovillard, N., Forel, M.B., Crasquin, S., 2015. Geochemistry of post-extinction microbialites as a powerful tool to assess the oxygenation of shallow marine water in the immediate aftermath of the end-Permian mass extinction. Int. J. Earth Sci. 104, 1025–1037. https://doi.org/10.1007/s00531-014-1125-3

Coshell, L., Rosen, M.R., 1994. Stratigraphy and Holocene History of Lake Hayward, Swan Coastal Plain Wetlands, western Australia. In: Renaut R. and Last W. (eds), Sedimentology and Geochemistry of Modern and Ancient Saline Lakes. SEPM, Tulsa, Sp. Publ. 50, 173–188.

De Boever, E., Birgel, D., Thiel, V., Muchez, P., Peckmann, J., Dimitrov, L., & Swennen, R., 2009. The formation of giant tubular concretions triggered by anaerobic oxidation of methane as revealed by archaeal molecular fossils (Lower Eocene, Varna, Bulgaria). Palaeogeography, Palaeoclimatology, Palaeoecology, 280(1-2), 23-36. https://doi.org/10.1016/j.palaeo.2009.05.010

Dellisanti, F., Pini, G.A., Baudin, F., 2010. Use of Tmax as a thermal maturity indicator in orogenic successions and comparison with clay mineral evolution. Clay Miner. 45, 115–130. https://doi.org/10.1180/claymin.2010.045.1.115

Dera, G., Brigaud, B., Monna, F., Laffont, R., Pucéat, E., Deconinck, J.-F., Pellenard, P., Joachimski, M.M., Durlet, C., 2011. Climatic ups and downs in a disturbed Jurassic world. Geology 39, 215–218. https://doi.org/10.1130/G31579.1

Droste, H., 1990. Depositional cycles and source rock development in an epeiric intra-platform basin: the Hanifa Formation of the Arabian peninsula. Sediment. Geol., Processes and Patterns in Epeiric Basins 69, 281–296. https://doi.org/10.1016/0037-0738(90)90054-W

Dupraz, C., Visscher, P.T., Baumgartner, L.K., Reid, R.P., 2004. Microbe–mineral interactions: early carbonate precipitation in a hypersaline lake (Eleuthera Island, Bahamas). Sedimentology 51, 745–765. https://doi.org/10.1111/j.1365-3091.2004.00649.x

948 Dupraz, C., Fowler, A., Tobias, C., Visscher, P.T., 2013. Stromatolitic knobs in Storr's Lake (San
949 Salvador, Bahamas): a model system for formation and alteration of laminae. Geobiology 11,
950 527–548. https://doi.org/10.1111/gbi.12063
951 Eltom, H.A., Rankey, E.C., Hasiotis, S.T., Gonzalez, L.A., Cantrell, D.A., 2017. Impact of Upwelling
952 On Heterozoan, Biosiliceous, and Organic-rich Deposits: Jurassic (oxfordian) Hanifa
953 Formation, Saudi Arabia. J. Sediment. Res. 87, 1235–1258.
954 https://doi.org/10.2110/jsr.2017.71
955 Enay, R., Le Nindre, Y-M., Mangold, C., Manivit, J., Vaslet, D., 1987. Le Jurassique d'Arabie
956 saoudite centrale. In, R. Enay (Ed.), Le Jurassique d'Arabie Saoudite Centrale. Geobios, Lyon,
957 Mémoire Spécial, no. 9, p. 13-65.
958 Espitalié, J., Deroo, G., Marquis, F., 1985. La pyrolyse Rock-Eval et ses applications. Première partie.
959 Rev. Inst. Fr. Pétrole 40, 563–579. https://doi.org/10.2516/ogst:1985035
960 Georgiev, S.V., Stein, H.J., Hannah, J.L., Xu, G., Bingen, B., Weiss, H.M., 2017. Timing, duration,
961 and causes for Late Jurassic–Early Cretaceous anoxia in the Barents Sea. Earth Planet. Sci.
962 Lett. 461, 151–162. https://doi.org/10.1016/j.epsl.2016.12.035
963 Glunk, C., Dupraz, C., Braissant, O., Gallagher, K. L., Verrecchia, E. P., Visscher, P. T., 2011.
964 Microbially mediated carbonate precipitation in a hypersaline lake, Big Pond (Eleuthera,
965 Bahamas). Sedimentology, 58(3), 720-736. https://doi.org/10.1111/j.1365-3091.2010.01180.x
966 Hammes, U., Hamlin, H.S., Ewing, T.E., 2011. Geologic analysis of the Upper Jurassic Haynesville
967 Shale in east Texas and west Louisiana. AAPG Bull. 95, 1643–1666.
968 https://doi.org/10.1306/02141110128
969 Hardenbol, J. A. N., Thierry, J., Farley, M. B., Jacquin, T., De Graciansky, P. C., & Vail, P. R., 1998.
970 Mesozoic and Cenozoic sequence chronostratigraphic framework of European basins.
971 Hardie, L.A., 1986. Ancient carbonate tidal-flat deposits. Colo. Sch. Mines Q. 81, 37–57.
972 Heydari, E., Wade, W.J., Anderson, L.C., 1997. Depositional Environments, Organic Carbon
973 Accumulation, and Solar-Forcing Cyclicity in Smackover Formation Lime Mudstones,
974 Northern Gulf Coast. AAPG Bull. 81, 760–774.
975 Himmler, T., Smrzka, D., Zwicker, J., Kasten, S., Shapiro, R.S., Bohrmann, G., Peckmann, J., 2018.
976 Stromatolites below the photic zone in the northern Arabian Sea formed by calcifying
977 chemotrophic microbial mats. Geology. https://doi.org/10.1130/G39890.1
978 Ilyn, V.D., Fortunatova, N.K., 1988. Methods of Prediction and Exploration in Oil and Gas Bearing
979 Reefal Complexes. Nedra 201, 200.
980 Immenhauser, A., Kenter, J.A.M., Ganssen, G., Bahamonde, J.R., Vliet, A.V., Saher, M.H., 2002.
981 Origin and Significance of Isotope Shifts in Pennsylvanian Carbonates (Asturias, NW Spain).
982 J. Sediment. Res. 72, 82–94. https://doi.org/10.1306/051701720082
983 Jadoul F., Berra F., Garzanti E., 1998. The Tethys Himalayan passive margin from Late Triassic to
984 Early Cretaceous (South Tibet). J. Asian Earth Sci. 16:173–194.
985 Jahnert, R.J., and Collins, L.B., 2012. Characteristics, distribution and morphogenesis of subtidal
986 microbial systems in Shark Bay, Australia. Marine Geology, v. 303–306, p. 115–136.
987 Jain, K.P., Garg, R., Kumar, S., Singh, I.B., 1984. Upper Jurassic dinoflagellate biostratigraphy of
988 Spiti Shale (Formation), Malla Johar area, Tethys Himalaya, India. J. Palaeontol. Soc. India
989 29, 67–83.
990 Jenkyns, H.C., 2003. Evidence for rapid climate change in the Mesozoic–Palaeogene greenhouse
991 world. Philos. Trans. R. Soc. Lond. Math. Phys. Eng. Sci. 361, 1885–1916.
992 https://doi.org/10.1098/rsta.2003.1240
993 Jones, C.E., Jenkyns, H.C., 2001. Seawater Strontium Isotopes, Oceanic Anoxic Events, and Seafloor
994 Hydrothermal Activity in the Jurassic and Cretaceous. Am. J. Sci. 301, 112–149.
995 https://doi.org/10.2475/ajs.301.2.112
996 Kirshin, A.V., 2007. Complex geological-geophysical researches of the Gissar block. Oil Gas Inst.
997 Tashkent.
998 Klett, T.R., Schenk, C.J., Wandrey, C.J., Charpentier, R.R., Brownfield, M.E., Pitman, J.K., Pollastro,
999 R.M., Cook, T.A., Tennyson, M.E., 2012. Assessment of undiscovered oil and gas resources
1000 of the Amu Darya Basin and Afghan-Tajik Basin Provinces, Afghanistan, Iran, Tajikistan,
1001 Turkmenistan, and Uzbekistan, 2011 (USGS Numbered Series No. 2011–3154), Fact Sheet.
1002 U.S. Geological Survey, Reston, VA.

Klett, T.R., Wandrey, C.J., Ulmishek, G.F., Amirzada, A., 2006. Afghan resource assessment fed positive outlook for exploration. Oil Gas J. 104.
Kuenen, J. G., 2008. Anammox bacteria: from discovery to application. Nature Reviews Microbiology, 6(4), 320.
Kuypers, M.M.M., Sliekers, A.O., Lavik, G., Schmid, M., Jørgensen, B.B., Kuenen, J.G., Damsté, J.S.S., Strous, M., Jetten, M.S.M., 2003. Anaerobic ammonium oxidation by anammox bacteria in the Black Sea. Nature, 422, 608-611.
Lézin, C., Andreu, B., Pellenard, P., Bouchez, J.-L., Emmanuel, L., Fauré, P., Landrein, P., 2013. Geochemical disturbance and paleoenvironmental changes during the Early Toarcian in NW Europe. Chem. Geol. 341, 1–15. https://doi.org/10.1016/j.chemgeo.2013.01.003
Lokier, S., Steuber, T., 2008. Quantification of Carbonate-Ramp Sedimentation and Progradation Rates for the Late Holocene Abu Dhabi Shoreline. J. Sediment. Res. 78, 423–431. https://doi.org/10.2110/jsr.2008.049
Lokier, S.W., Andrade, L.L., Court, W.M., Dutton, K.E., Head, I.M., Land, C. van der, Paul, A., Sherry, A., 2017. A new model for the formation of microbial polygons in a coastal sabkha setting. Depositional Rec. 3, 201–208. https://doi.org/10.1002/dep2.33
Louis-Schmid, B., Rais, P., Bernasconi, S.M., Pellenard, P., Collin, P.-Y., Weissert, H., 2007. Detailed record of the mid-Oxfordian (Late Jurassic) positive carbon-isotope excursion in two hemipelagic sections (France and Switzerland): A plate tectonic trigger? Palaeogeogr. Palaeoclimatol. Palaeoecol. 248, 459–472. https://doi.org/10.1016/j.palaeo.2007.01.001
Marshall, J.D., 1992. Climatic and oceanographic isotopic signals from the carbonate rock record and their preservation. Geol. Mag. 129, 143–160. https://doi.org/10.1017/S0016756800008244
Martinez, M., Dera, G., 2015. Orbital pacing of carbon fluxes by a ~9-My eccentricity cycle during the Mesozoic. Proc. Natl. Acad. Sci. 112, 12604–12609. https://doi.org/10.1073/pnas.1419946112
McArthur, A.D., Kneller, B.C., Souza, P.A., Kuchle, J., 2016. Characterization of deep-marine channel-levee complex architecture with palynofacies: An outcrop example from the Rosario Formation, Baja California, Mexico. Mar. Pet. Geol. 73, 157–173. https://doi.org/10.1016/j.marpetgeo.2016.02.030
McKirdy, D.M., Padley, D., MacDonald, F., Warren, J., Hayball, A., Von Der Borch, C., 1992. Coorong lacustrine carbonates as analogues of ancient evaporite-associated hydrocarbon source rocks, in: AAPG International Conference and Exhibition, Sydney, Abstracts. pp. 63–64.
McLennan, S.M., 2001. Relationships between the trace element composition of sedimentary rocks and upper continental crust. Geochem. Geophys. Geosystems 2. https://doi.org/10.1029/2000GC000109
Meer, D.G.V.D., Zeebe, R.E., Hinsbergen, D.J.J. van, Sluijs, A., Spakman, W., Torsvik, T.H., 2014. Plate tectonic controls on atmospheric CO2 levels since the Triassic. Proc. Natl. Acad. Sci. 201315657. https://doi.org/10.1073/pnas.1315657111
Mirkamalov, H.H., Abdullaev, G.S., Evseeva, G.B., Sudareva, E.U., Ahmedova, M.R., Haneeva, F.R., Muratova, L.M., 2005. The studying of the Jurassic sediments of the Beshkent trough and nearby areas to precise its lithological-facial and stratigraphic structure and to determine its relations with the pre-Mesozoic complexes. Report, Oil and Gas Institute, Tashkent (in Russian). 111.
Mitta, V.V., 1992. Callovian Pachyceratids (Ammonoidea) Of Central Asia. Paleontol. J. 26, 4.
Mitta, V.V., Besnosov, N.V., 2007. Jurassic System Cephalopods. Palaeontol. Atlas Phaneroz. Faunas Floras Uzb. Volume II Mesoz. Cenozoic Jurass. Cretac. Palaeogene, Republic of Uzbekistan State Committee on Geology and Mineral Resources, Tashkent, Uzbekistan.
Moore, D.M., Reynolds, R.C., 1989. X-ray Diffraction and the Identification and Analysis of Clay Minerals. Oxford university press New York.
Mordvintsev, D., 2015. Tectono-stratigraphic evolution of the northern margin of the Amu-Darya basin in Uzbekistan (Bukhara-Khiva and Southwestern Gissar regions). PhD thesis. University P. & M. Curie, Paris, France.

Mukhopadhyay, P. K., Wade, J. A., & Kruge, M. A., 1997. Source Rocks for Condensate and Gas-Examples from Jurassic-Cretaceous Sediments of Scotian Basin, Nova Scotia, Eastern Canada.

Nugmanov, A.H., 2010. Laws of formation of traps and oil and gas fields, oil and gas potential of the northern side of the Amu-Darya syncline. Geology Geophysics Institute, Tashkent, Uzbekistan.

O'Dogherty, L., Aguado, R., Baumgartner, P.O., Bill, M., Goričan, Š., Sandoval, J., Sequeiros, L., 2018. Carbon-isotope stratigraphy and pelagic biofacies of the Middle–Upper Jurassic transition in the Tethys–Central Atlantic connection. Palaeogeogr. Palaeoclimatol. Palaeoecol. 507, 129–144. https://doi.org/10.1016/j.palaeo.2018.07.006

Oehler, J.H., 1984. Carbonate Source Rocks in the Jurassic Smackover Trend of Mississippi, Alabama, and Florida 30, 63–69.

Olivero, E.B., Raffi, M.E., 2018. Onshore–offshore trends in Campanian ammonite facies from the Marambio Group, Antarctica: Implications for ammonite habitats. Cretac. Res., Cretaceous ammonites: a volume in memory of Richard A. Reyment (1926–2016) 88, 79–89. https://doi.org/10.1016/j.cretres.2017.03.001

Pace, A., Bourillot, R., Bouton, A., Vennin, E., Braissant, O., Dupraz, C., Duteil, T., Bundeleva, I., Patrier, P., Galaup, S., Yokoyama, Y., Franceschi, M., Virgone, A., Visscher, P.T., 2018. Formation of stromatolite lamina at the interface of oxygenic–anoxygenic photosynthesis. Geobiology 16, 378–398. https://doi.org/10.1111/gbi.12281

Padden, M., Weissert, H., Rafelis, M. de, 2001. Evidence for Late Jurassic release of methane from gas hydrate. Geology 29, 223–226. https://doi.org/10.1130/0091-7613(2001)029<0223:EFLJRO>2.0.CO;2

Palma, R., Bressan, G.S., Kietzmann, D.A., Riccardi, A.C., Martín-Chivelet, J., López-Gómez, J., 2014. Palaeoenvironmental significance of middle Oxfordian deep marine deposits from La Manga Formation, Neuquén Basin, Argentina. J. Iber. Geol. 40, 507–520. https://doi.org/10.5209/rev_JIGE.2014.v40.n3.43804

Palma, R., Kietzmann, D.A., Comerio, M., Martín-Chivelet, J., López-Gómez, J., Bressan, G.S., 2015. Oxfordian microbial laminites from La Manga Formation, Neuquén Basin, Argentina: Remarkable nanobacteria preservation.

Pearce, C.R., Hesselbo, S.P., Coe, A.L., 2005. The mid-Oxfordian (Late Jurassic) positive carbon-isotope excursion recognised from fossil wood in the British Isles. Palaeogeogr. Palaeoclimatol. Palaeoecol. 221, 343–357. https://doi.org/10.1016/j.palaeo.2005.03.004

Pellenard, P., Deconinck, J.-F., 2006. Mineralogical variability of Callovo-Oxfordian clays from the Paris Basin and the Subalpine Basin. Comptes Rendus Geosci., Le Callovo-Oxfordien du bassin de Paris : du contexte géologique à la modélisation de ses propriétés 338, 854–866. https://doi.org/10.1016/j.crte.2006.05.008

Pellenard, P., Tramoy, R., Pucéat, E., Huret, E., Martinez, M., Bruneau, L., Thierry, J., 2014. Carbon cycle and sea-water palaeotemperature evolution at the Middle–Late Jurassic transition, eastern Paris Basin (France). Mar. Pet. Geol., Present and past transfers in a sedimentary aquifer – aquitard system: a 2000 meter deep drill-hole in the Mesozoic of the Paris Basin 53, 30–43. https://doi.org/10.1016/j.marpetgeo.2013.07.002

Petschick, R., 2001. 'MacDiff 4.2.5 manual.' (Johann Wolfgang Goethe-Universitat Frankfurt am Main: Frankfurt)

Quan, T.M., Falkowski, P.G., 2009. Redox control of N:P ratios in aquatic ecosystems. Geobiology 7, 124–139. doi:10.1111/j.1472-4669.2008.00182.x

Rais, P., Louis-Schmid, B., Bernasconi, S.M., Weissert, H., 2007. Palaeoceanographic and palaeoclimatic reorganization around the Middle–Late Jurassic transition. Palaeogeogr. Palaeoclimatol. Palaeoecol. 251, 527–546. https://doi.org/10.1016/j.palaeo.2007.05.008

Raven, M. R., Fike, D. A., Gomes, M. L., Webb, S. M., 2019. Chemical and isotopic evidence for organic matter sulfurization in redox gradients around mangrove roots. Frontiers in Earth Science, 7, 98. https://doi.org/10.3389/feart.2019.00098

Reeburgh, W.S., 2007. Oceanic Methane Biogeochemistry. Chem. Rev. 107, 486–513. https://doi.org/10.1021/cr050362v

Rickard, D., Mussmann, M., Steadman, J.A., 2017. Sedimentary Sulfides. Elements 13, 117–122. https://doi.org/10.2113/gselements.13.2.117
Rita, P., Reolid, M., Duarte, L.V., 2016. Benthic foraminiferal assemblages record major environmental perturbations during the Late Pliensbachian–Early Toarcian interval in the Peniche GSSP, Portugal. Palaeogeogr. Palaeoclimatol. Palaeoecol. 454, 267–281. https://doi.org/10.1016/j.palaeo.2016.04.039
Schnyder, J., Ruffell, A., Deconinck, J.-F., Baudin, F., 2006. Conjunctive use of spectral gamma-ray logs and clay mineralogy in defining late Jurassic–early Cretaceous palaeoclimate change (Dorset, U.K.). Palaeogeogr. Palaeoclimatol. Palaeoecol. 229, 303–320. https://doi.org/10.1016/j.palaeo.2005.06.027
Schnyder, J., Baudin, F., Deconinck, J.-F., 2009. Occurrence of organic-matter-rich beds in Early Cretaceous coastal evaporitic setting (Dorset, UK): a link to long-term palaeoclimate changes? Cretac. Res. 30, 356–366. https://doi.org/10.1016/j.cretres.2008.07.014
Schnyder, J., Stetten, E., Baudin, F., Pruski, A.M., Martinez, P., 2017. Palynofacies reveal fresh terrestrial organic matter inputs in the terminal lobes of the Congo deep-sea fan. Deep Sea Res. Part II Top. Stud. Oceanogr., Organic carbon transfer and ecosystem functioning in the terminal lobes of the Congo deep-sea fan: The Conglobe multidisciplinary study 142, 91–108. https://doi.org/10.1016/j.dsr2.2017.05.008
Sharland, P., Archer, R., Casey, D.M., Davies, R.B., Hall, S.H., Heward, A.P., Horbury, A.D., Simmons, M. 2001. Arabian Plate Sequence Stratigraphy. GeoArabia Special Publication, 2 372p.
Shawar, L., Halevy, I., Said-Ahmad, W., Feinstein, S., Boyko, V., Kamyshny, A., Amrani, A., 2018. Dynamics of pyrite formation and organic matter sulfurization in organic-rich carbonate sediments. Geochimica et Cosmochimica Acta, 241, 219-239. https://doi.org/10.1016/j.gca.2018.08.048
Shearman, D.J., 1966. Origin of marine evaporites by diagenesis. Trans Inst Min Met. 75, 208–215.
Storme, J.-Y., Dupuis, C., Schnyder, J., Quesnel, F., Garel, S., Iakovleva, A.I., Iacumin, P., Di Matteo, A., Sebilo, M., Yans, J., 2012. Cycles of humid-dry climate conditions around the P/E boundary: new stable isotope data from terrestrial organic matter in Vasterival section (NW France). Terra Nova 24, 114–122. https://doi.org/10.1111/j.1365-3121.2011.01044.x
Sucha, V., Kraus, I., Gerthofferova, H., Petes, J., Serekova, M., 1993. Smectite to illite conversion in bentonites and shales of the East Slovak Basin. Clay Miner. 28, 243–243. https://doi.org/10.1180/claymin.1993.028.2.06
Trabucho-Alexandre, J., Dirkx, R., Veld, H., Klaver, G., & de Boer, P. L., 2012.Toarcian black shales in the Dutch Central Graben: record of energetic, variable depositional conditions during an oceanic anoxic event. Journal of sedimentary Research, 82(2), 104-120. https://doi.org/10.2110/jsr.2012.5
Tribovillard, N., Desprairies, A., Lallier-Vergès, E., Bertrand, P., Moureau, N., Ramdani, A., Ramanampisoa, L., 1994. Geochemical study of organic-matter rich cycles from the Kimmeridge Clay Formation of Yorkshire (UK): productivity versus anoxia. Palaeogeogr. Palaeoclimatol. Palaeoecol. 108, 165–181. https://doi.org/10.1016/0031-0182(94)90028-0
Tribovillard, N., Trentesaux, A., Trichet, J., Défarge, C., 2000. A Jurassic counterpart for modern kopara of the Pacific atolls: lagoonal, organic matter-rich, laminated carbonate of Orbagnoux (Jura Mountains, France). Palaeogeogr. Palaeoclimatol. Palaeoecol. 156, 277–288. https://doi.org/10.1016/S0031-0182(99)00145-5
Tribovillard, N., Riboulleau, A., Lyons, T., Baudin, F., 2004. Enhanced trapping of molybdenum by sulfurized marine organic matter of marine origin in Mesozoic limestones and shales. Chemical Geology, 213(4), 385-401. https://doi.org/10.1016/j.chemgeo.2004.08.011
Tribovillard, N., Algeo, T.J., Lyons, T., Riboulleau, A., 2006. Trace metals as paleoredox and paleoproductivity proxies: An update. Chem. Geol. 232, 12–32. https://doi.org/10.1016/j.chemgeo.2006.02.012
Tyson, R.V., 1995. Abundance of Organic Matter in Sediments: TOC, Hydrodynamic Equivalence, Dilution and Flux Effects, in: Sedimentary Organic Matter. Springer, Dordrecht, pp. 81–118. https://doi.org/10.1007/978-94-011-0739-6_5

Tyson, R.V., 2012. Sedimentary organic matter: organic facies and palynofacies. Springer Science & Business Media.
Ulmishek, G.F., 2004. Petroleum geology and resources of the Amu-Darya basin, Turkmenistan, Uzbekistan, Afghanistan, and Iran (USGS Numbered Series No. 2201- H), Bulletin.
Vahrenkamp, V.C., Van Laer, P., Franco, B., Celentano, M.A., Grelaud, C., Razin, P., 2015. Late Jurassic to Cretaceous Source Rock Prone Intra-Shelf Basins of the Eastern Arabian Plate–Interplay between Tectonism, Global Anoxic Events and Carbonate Platform Dynamics, in: International Petroleum Technology Conference.
Vasconcelos, C., Warthmann, R., McKenzie, J. A., Visscher, P. T., Bittermann, A. G., van Lith, Y. 2006. Lithifying microbial mats in Lagoa Vermelha, Brazil: modern Precambrian relics?. Sedimentary Geology, 185(3-4), 175-183. https://doi.org/10.1016/j.sedgeo.2005.12.022
Visscher, P.T., Stolz, J.F., 2005. Microbial mats as bioreactors: populations, processes, and products, in: Noffke, N. (Ed.), Geobiology: Objectives, Concepts, Perspectives. Elsevier, Amsterdam, pp. 87–100. https://doi.org/10.1016/B978-0-444-52019-7.50009-7
Warren, J.K., 2011. Evaporitic source rocks: mesohaline responses to cycles of "famine or feast" in layered brines. Int Assoc Sediment Spec Publ 43, 315–392.
West, I.M., 1975. Evaporites and associated sediments of the basal Purbeck Formation (Upper Jurassic) of Dorset. Proc. Geol. Assoc. 86, 205–225. https://doi.org/10.1016/S0016-7878(75)80101-5
Whitaker, M.F., Giles, M.R., Cannon, S.J.C., 1992. Palynological review of the Brent Group, UK sector, north sea. Geol. Soc. Lond. Spec. Publ. 61, 169–202. https://doi.org/10.1144/GSL.SP.1992.061.01.10
Wilson, J.L., 1975. Carbonate Facies in Geologic History. Springer.

FIGURE LEGENDS

Fig. 1: A) Location of the Amu Darya and Afghan-Tajik basins in western Central Asia. ADF, Amu Darya Fault; C Ust F, Central Ustyurt Fault; STS F, South Tien Shan Fault; UKFFZ, Uchbash-Karshi Flexure Fault Zone; Za F, Zaravshan Fault. **B)** Location of the Tubiegatan section in the SW Gissar Range and geological setting of the study area (Surkhandarya province). Gau, Gaurdak section. **C-D)** View of the Khodjaipak Fm. in the Tubiegatan section (C) and of the Tubiegatan anticline (D).

Fig. 2: Simplified stratigraphic chart of the Middle–Upper Jurassic formations in the NE part of the Amu Darya Basin based on the works carried out by Fürsich et al., 2017, Carmeille et al., 2018 and this study.

Fig. 3: Sedimentological section of the Kugitang carbonates and the Khodjaipak Formation in the Tubiegatan area. The vertical variations of bulk mineralogy, clay-mineral assemblages and Total Organic Carbon (TOC) are plotted along the section. High frequency transgressive-regressive cycles and ammonite biostratigraphy are indicated to the left side. For the location of the section, refer to Fig. 1B.

Fig. 4: Sedimentary facies of the Tubiegatan section: **A)** Ammonite imprint at the surface of a bioturbated horizon, lower carbonate interval; **B-C)** Examples of *Thalassinoides* burrows (Bur.) in the limestones, lower carbonate interval (F2b); **D)** Black to brownish marls to siltstones (F1a), Khodjaipak Fm; **E)** Black nodule of organic-rich mud-carbonate, intercalated in brown marls to siltstones (F1b), Khodjaipak Fm; **F)** Shell (storm?) bed (F1d) composed of disarticulated bivalves and brachiopod fragments, Khodjaipak Fm.

Fig. 5: Laminated organic microbial boundstone (F1c), Khodjaipak Fm.: **A-B)** Alternation of millimetric and infra-millimetric carbonate and organic lamina. Note the occurrence of sulfate pseudomorphs in B (yellow arrows). **C)** Laminae composed of organic-rich carbonate peloids (orange arrow). **D)** Planktonic foraminifera trapped in a stromatolite lamina. **E)** Detail of an organic-carbonate mineral couplet. Organic matter is concentrated in the organic-rich laminae, but also between the microspar crystals of the carbonate laminae. **F)** Yellow to brown aggregates (yellow arrow), which could be hydrocarbon droplets. A is a field photograph, B is a scanned thin section and C to F are polarizing microscope images (plane polarized light).

Fig. 6: SEM images and EDS elemental mapping in the organic microbial boundstone (F1c). **A-B)** Micritic to microsparitic peloids in an alveolar organic network (A) and EDS element mapping (B). On the EDS map, calcite peloids are green (Ca-rich), the alveolar organic matrix (probable EPS remnants) is pink (C-rich), while clays are grey (Al-rich). **C)**. Close-up view of Fig. 6A. **D)** Organic matter-clay aggregate. Small bright sulfur rich globules (SG) are also locally observed. **E-F)** SEM picture (E) and EDS map (F) of a peloidal lamina. Calcite peloids (green) are surrounded by a mix of quartz (Si-rich; blue), clay (grey) and iron oxides (red).

Fig. 7: Hydrogen index (HI) versus T_{max} diagram. Circle diameter is proportional to TOC, and their color is related to the palynofacies intervals defined on Figure 8.

Fig. 8: Vertical evolution of palynofacies. DBW, degraded brown wood; AOM, amorphous organic matter; DSOM, dark structureless organic matter; WPFP, well-preserved wood fragments. **A to D)** Palynofacies photomicrographs. **A-B)** Orange to dark amorphous organic matter (AOM), sample 09-E3, 37.2 m. **C)** Dark AOM with rectangular shape, sample 09-E2, 37 m. **D)** Translucent phytoclasts, sample 13-E4, 21 m.

Fig. 9: Vertical evolution of organic ($\delta^{13}C_{org}$), inorganic ($\delta^{13}C_{carb}$ and $\delta^{18}O_{carb}$) and total ($\delta^{15}N_{tot}$) isotope ratio along the Tubiegatan section.

Fig. 10: $\delta^{13}C_{carb}$-$\delta^{18}O_{carb}$ cross-plots for the Tubiegatan section: Khodjaipak Fm., lower and upper carbonate intervals. The range of values for the south west Gissar platform carbonates (Callovian Sequence in green; Upper Jurassic Sequence in pink) are indicated.

Fig. 11: Vertical evolution of TOC, Mo_{xs} and some trace metal elemental ratios: U/Th and V/Cr along the Khodjaipak Fm. Within grey intervals (AI1 and AI2), the ratios point to anoxic conditions.

Fig. 12: Two correlation hypotheses between the Tubiegatan section and the south-west Gissar platform, based on the $\delta^{13}C_{carb}$ and the sequence stratigraphy.

Fig. 13: (A) Depositional scenario and **(B)** geomicrobiological model for the Khodjaipak Fm. in the Tubiegatan area, and relationship with the SW Gissar carbonate platform.

Fig. 14: Age, composition and distribution of the OM-rich sedimentary formation during the Oxfordian-Early Kimmeridgian period. The second-order NW Tethyan T/R cycles are from Hardenbol et al, 1998. The smoothed $\delta^{13}C_{carb}$ curve is from Martinez and Dera, 2015.

Fig. S1: A) Plot of $CaCO_3$ vs. TOC values for the Tubiegatan samples. Note that the highest values are associated to carbonate samples. **B-C)** Kaolinite vs. TOC: **(B)** percentage of kaolinite relative to bulk rock and **(C)** percentage of kaolinite relative to the clay fraction. **D)** R1-type illite-smectite mixed-layer (IS-R1) vs. TOC. The percentage of IS-R1 is relative to the clay fraction.

Fig. S2: Van Krevelen diagram: Hydrogen index (HI) vs. oxygen index (OI).

Fig. S3: Vertical evolution of the C/N ratio.

Figures

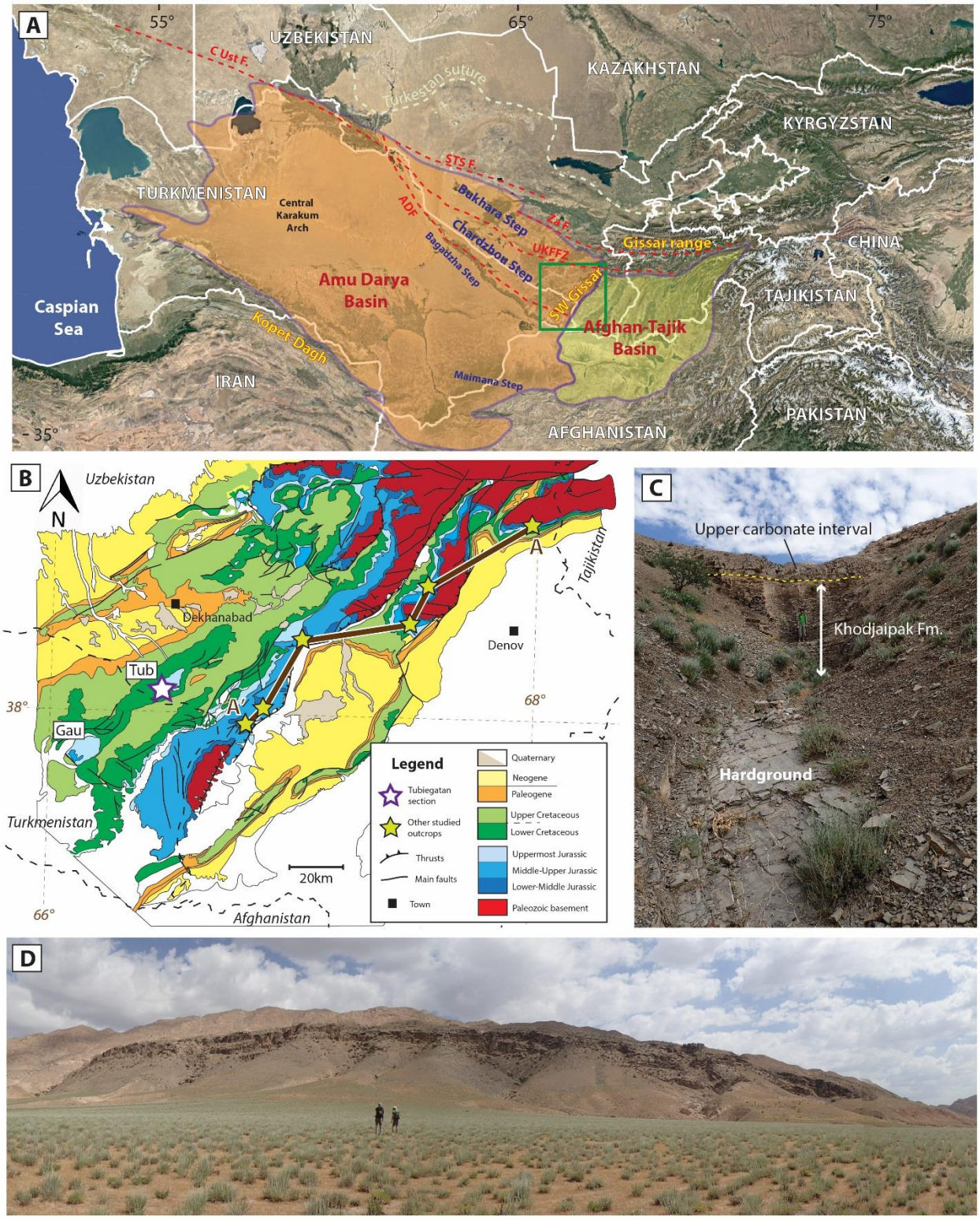

Fig. 1: A) Location of the Amu Darya and Afghan-Tajik basins in western Central Asia. ADF, Amu Darya Fault; C Ust F, Central Ustyurt Fault; STS F, South Tien Shan Fault; UKFFZ, Uchbash-Karshi Flexure Fault Zone; Za F, Zaravshan Fault. **B)** Location of the Tubiegatan section in the SW Gissar Range and geological setting of the study area (Surkhandarya province). Gau, Gaurdak section. **C-D)** View of the Khodjaipak Fm. in the Tubiegatan section (C) and of the Tubiegatan anticline (D).

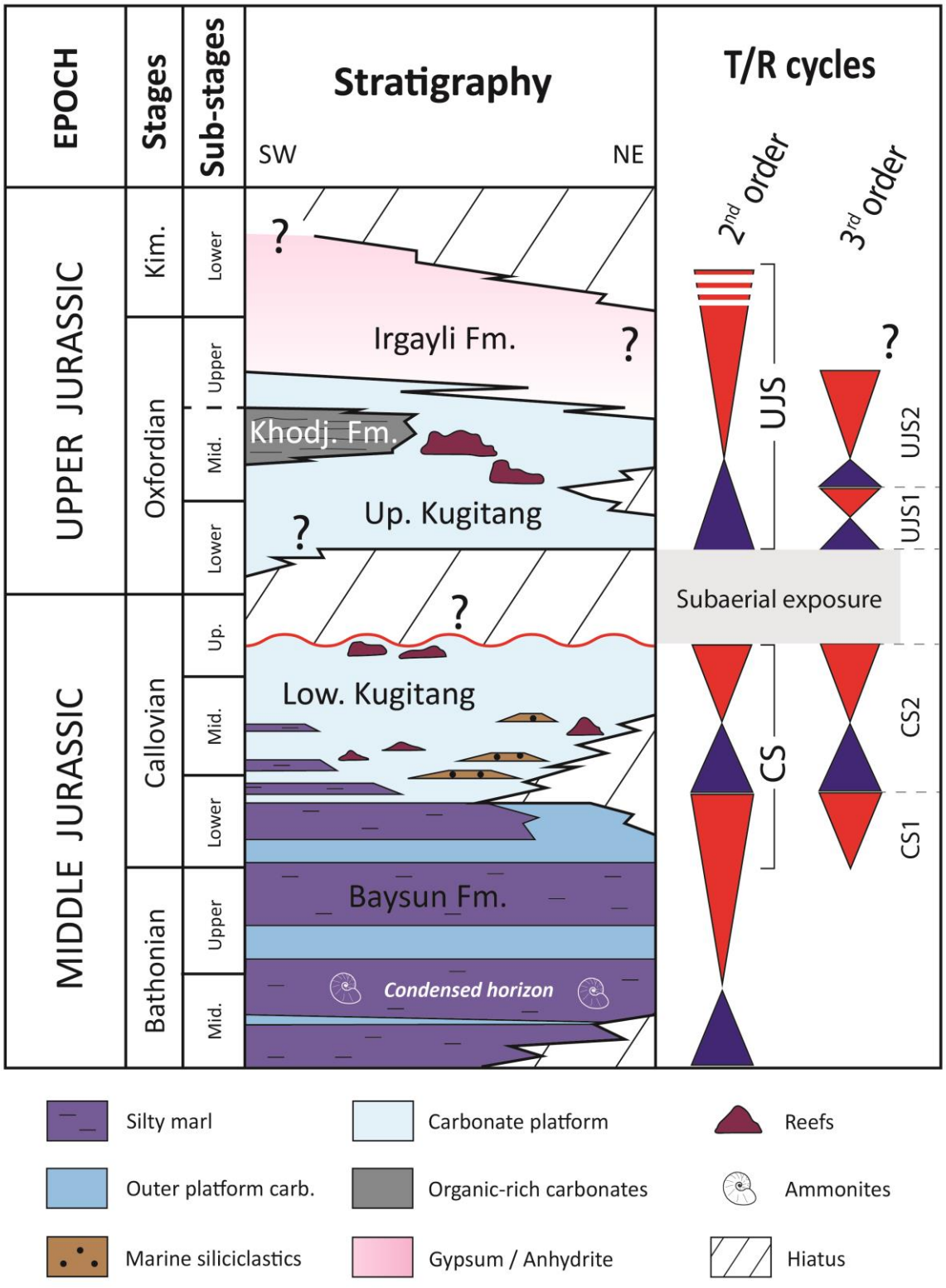

Fig. 2: Simplified stratigraphic chart of the Middle–Upper Jurassic formations in the NE part of the Amu Darya Basin based on the works carried out by Fürsich et al., 2017, Carmeille et al., 2018 and this study.

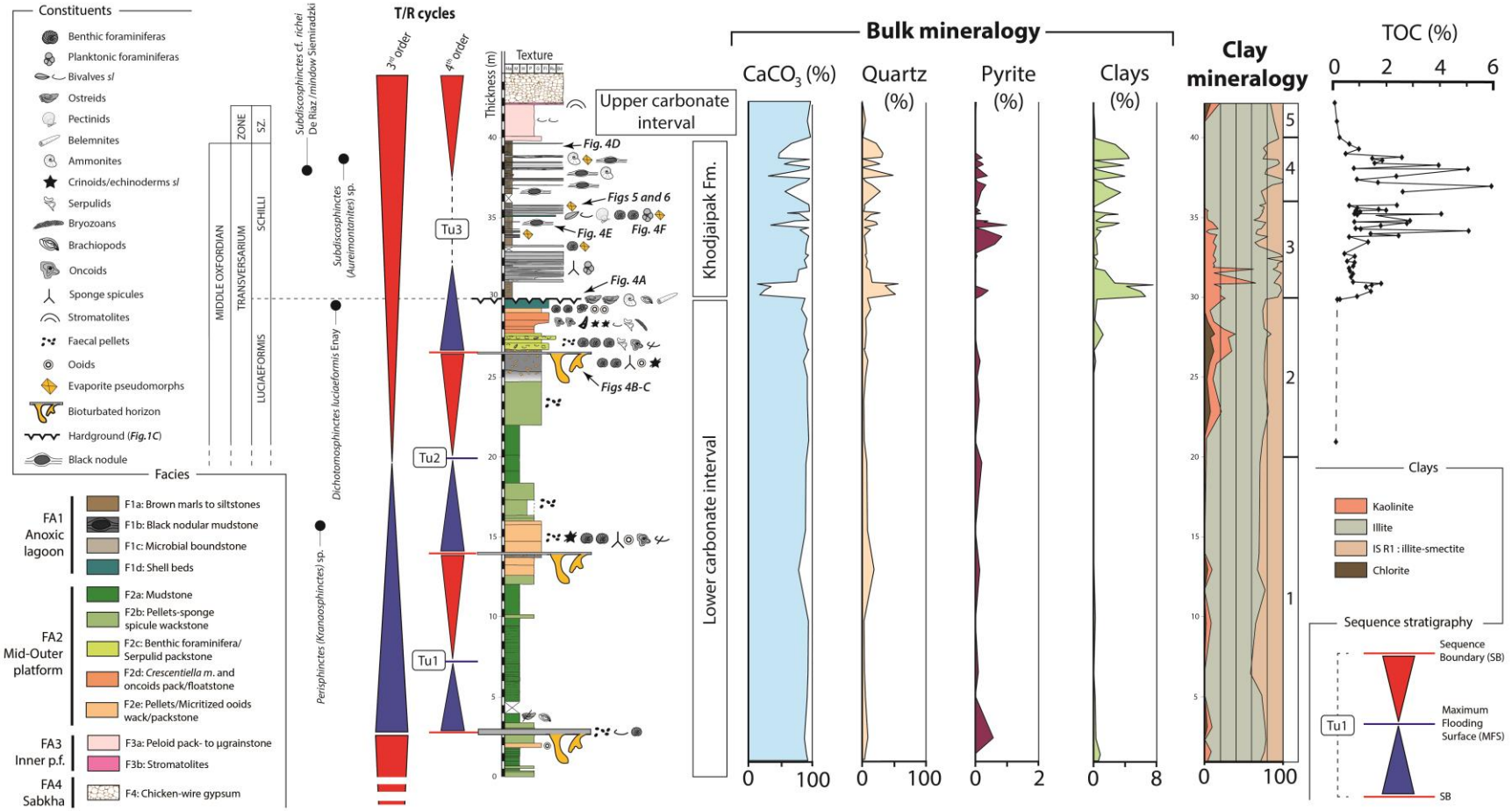

Fig. 3: Sedimentological section of the Kugitang carbonates and the Khodjaipak Formation in the Tubiegatan area. The vertical variations of bulk mineralogy, clay-mineral assemblages and Total Organic Carbon (TOC) are plotted along the section. High frequency transgressive-regressive cycles and ammonite biostratigraphy are indicated to the left side. For the location of the section, refer to Fig. 1B.

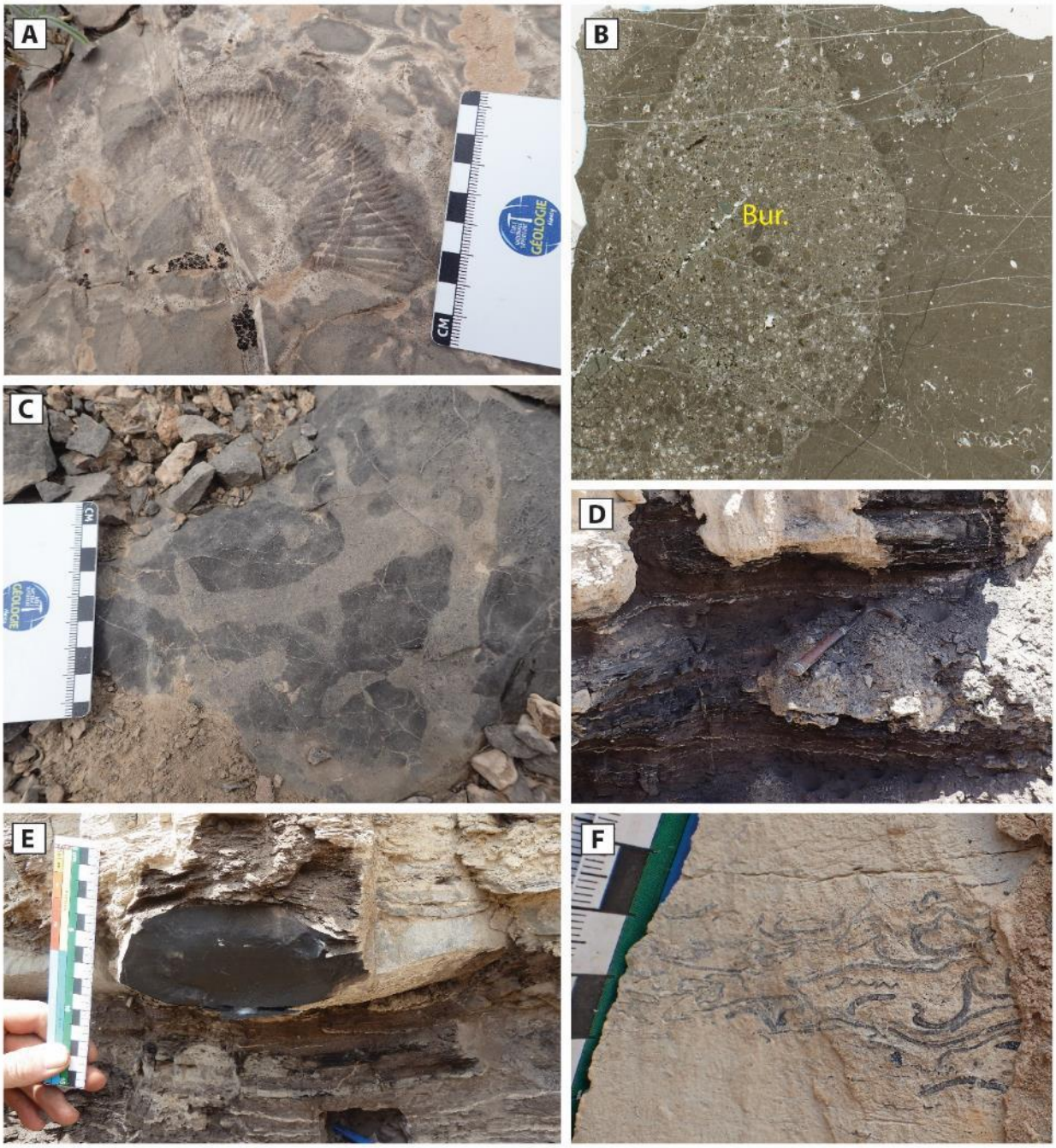

Fig. 4: Sedimentary facies of the Tubiegatan section: **A)** Ammonite imprint at the surface of a bioturbated horizon, lower carbonate interval; **B-C)** Examples of *Thalassinoides* burrows (Bur.) in the limestones, lower carbonate interval (F2b); **D)** Black to brownish marls to siltstones (F1a), Khodjaipak Fm; **E)** Black nodule of organic-rich mud-carbonate, intercalated in brown marls to siltstones (F1b), Khodjaipak Fm; **F)** Shell (storm?) bed (F1d) composed of disarticulated bivalves and brachiopod fragments, Khodjaipak Fm.

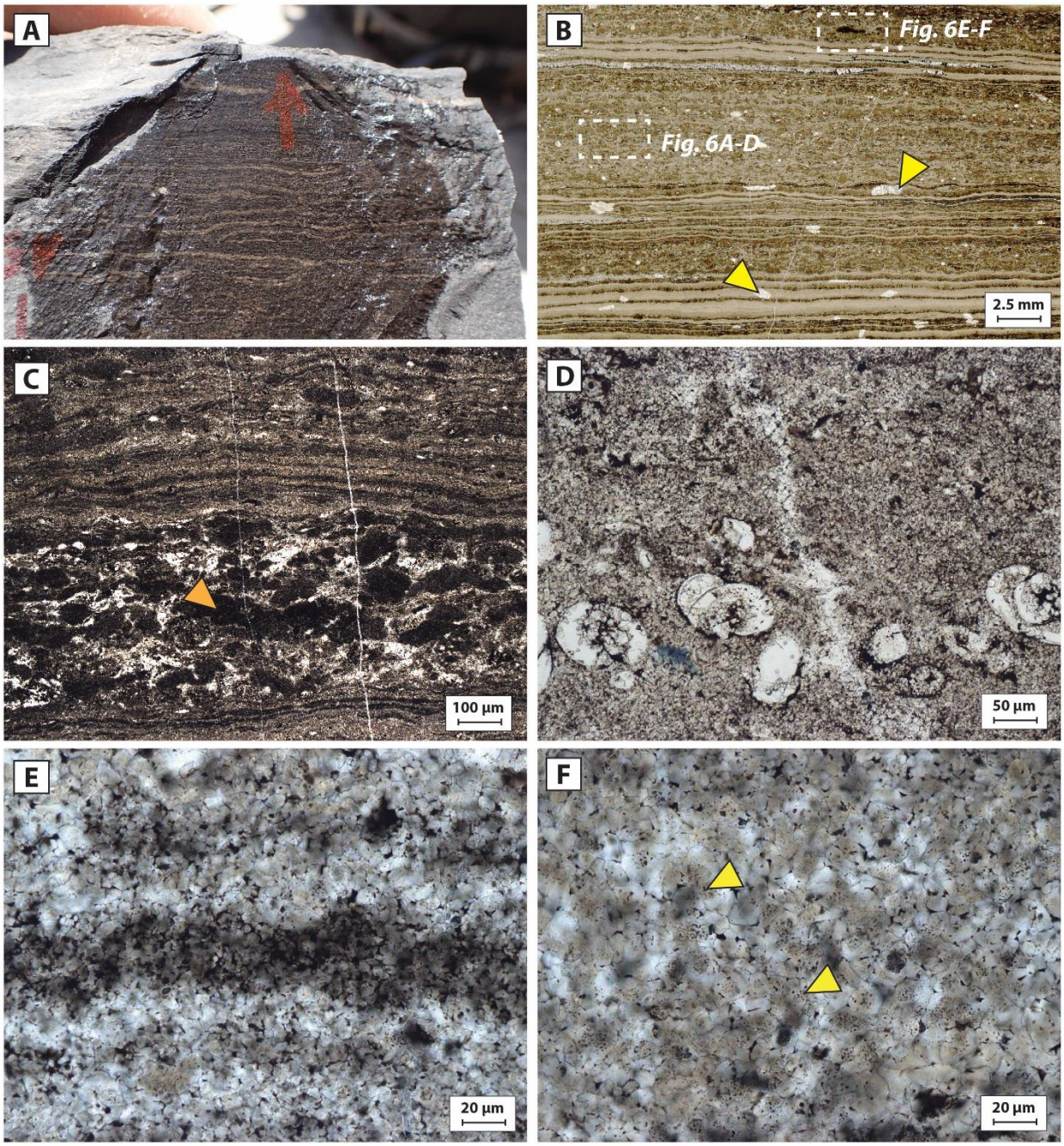

Fig. 5: Laminated organic microbial boundstone (F1c), Khodjaipak Fm.: **A-B)** Alternation of millimetric and infra-millimetric carbonate and organic lamina. Note the occurrence of sulfate pseudomorphs in B (yellow arrows). **C)** Laminae composed of organic-rich carbonate peloids (orange arrow). **D)** Planktonic foraminifera trapped in a stromatolite lamina. **E)** Detail of an organic-carbonate mineral couplet. Organic matter is concentrated in the organic-rich laminae, but also between the microspar crystals of the carbonate laminae. **F)** Yellow to brown aggregates (yellow arrow), which could be hydrocarbon droplets. A is a field photograph, B is a scanned thin section and C to F are polarizing microscope images (plane polarized light).

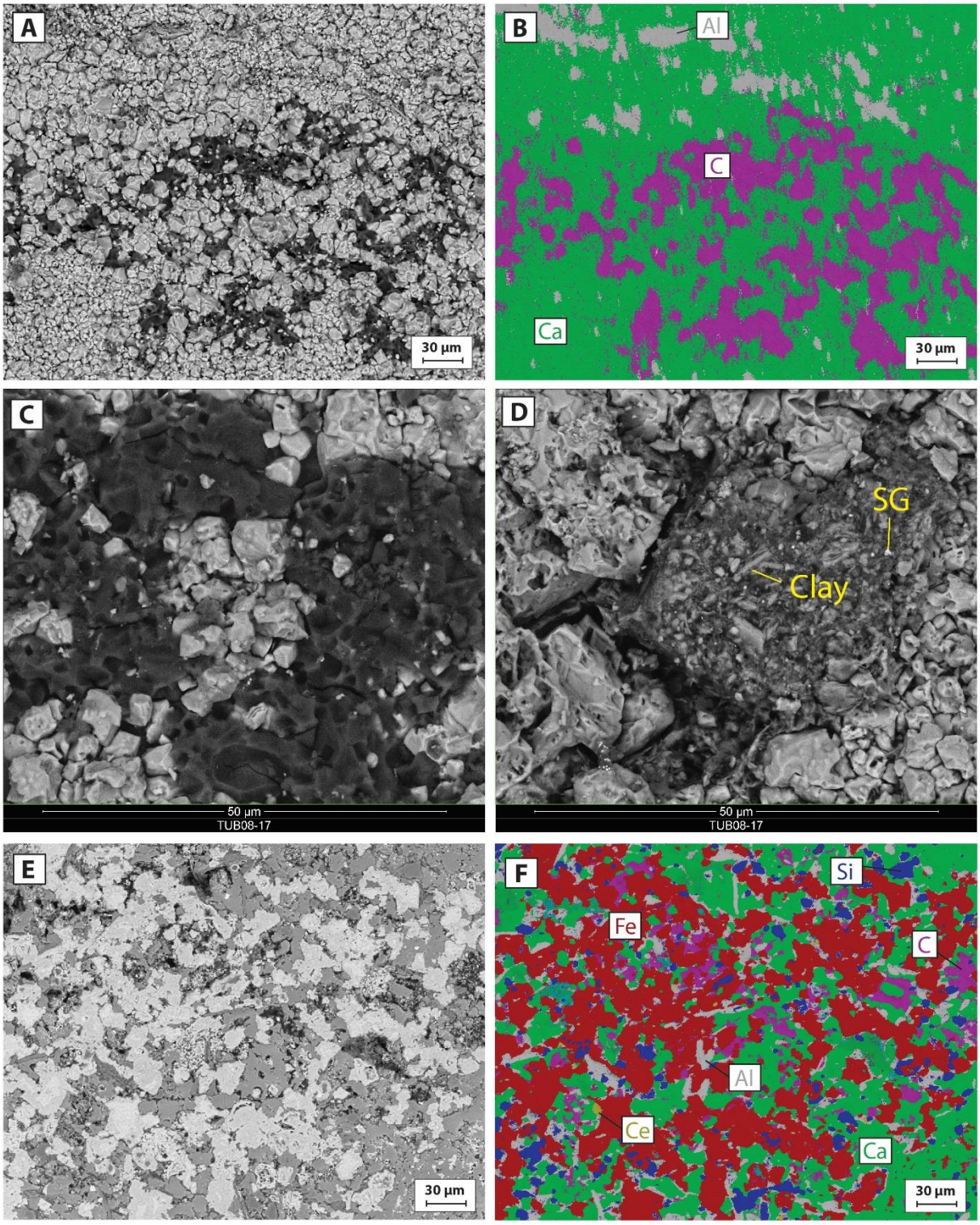

Fig. 6: SEM images and EDS elemental mapping in the organic microbial boundstone (F1c). **A-B)** Micritic to microsparitic peloids in an alveolar organic network (A) and EDS element mapping (B). On the EDS map, calcite peloids are green (Ca-rich), the alveolar organic matrix (probable EPS remnants) is pink (C-rich), while clays are grey (Al-rich). **C)**. Close-up view of Fig. 6A. **D)** Organic matter-clay aggregate. Small bright sulfur rich globules (SG) are also locally observed. **E-F)** SEM picture (E) and EDS map (F) of a peloidal lamina. Calcite peloids (green) are surrounded by a mix of quartz (Si-rich; blue), clay (grey) and iron oxides (red).

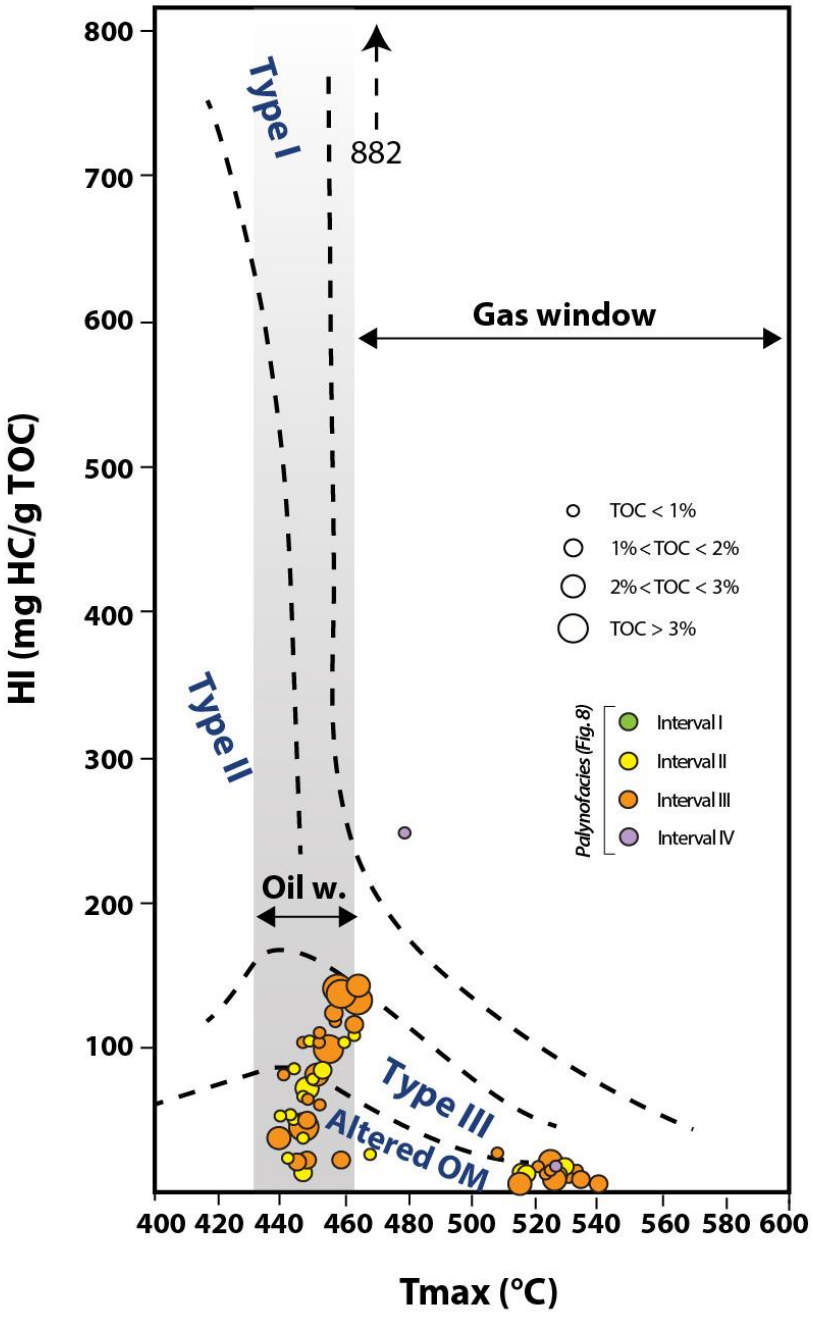

Fig. 7: Hydrogen index (HI) versus T_{max} diagram. Circle diameter is proportional to TOC, and their color is related to the palynofacies intervals defined on Figure 8.

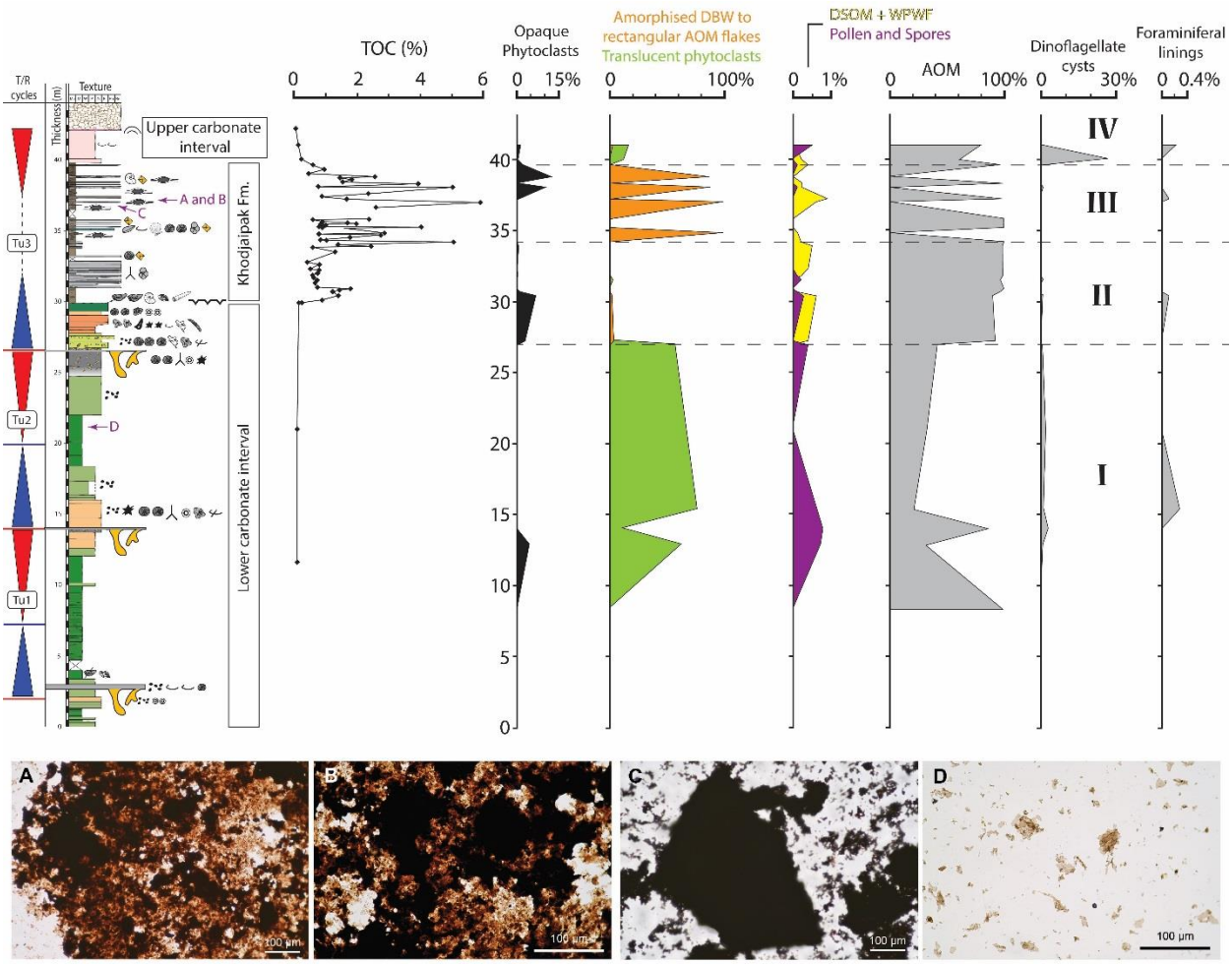

Fig. 8: Vertical evolution of palynofacies. DBW, degraded brown wood; AOM, amorphous organic matter; DSOM, dark structureless organic matter; WPFP, well-preserved wood fragments. **A to D)** Palynofacies photomicrographs. **A-B)** Orange to dark amorphous organic matter (AOM), sample 09-E3, 37.2 m. **C)** Dark AOM with rectangular shape, sample 09-E2, 37 m. **D)** Translucent phytoclasts, sample 13-E4, 21 m.

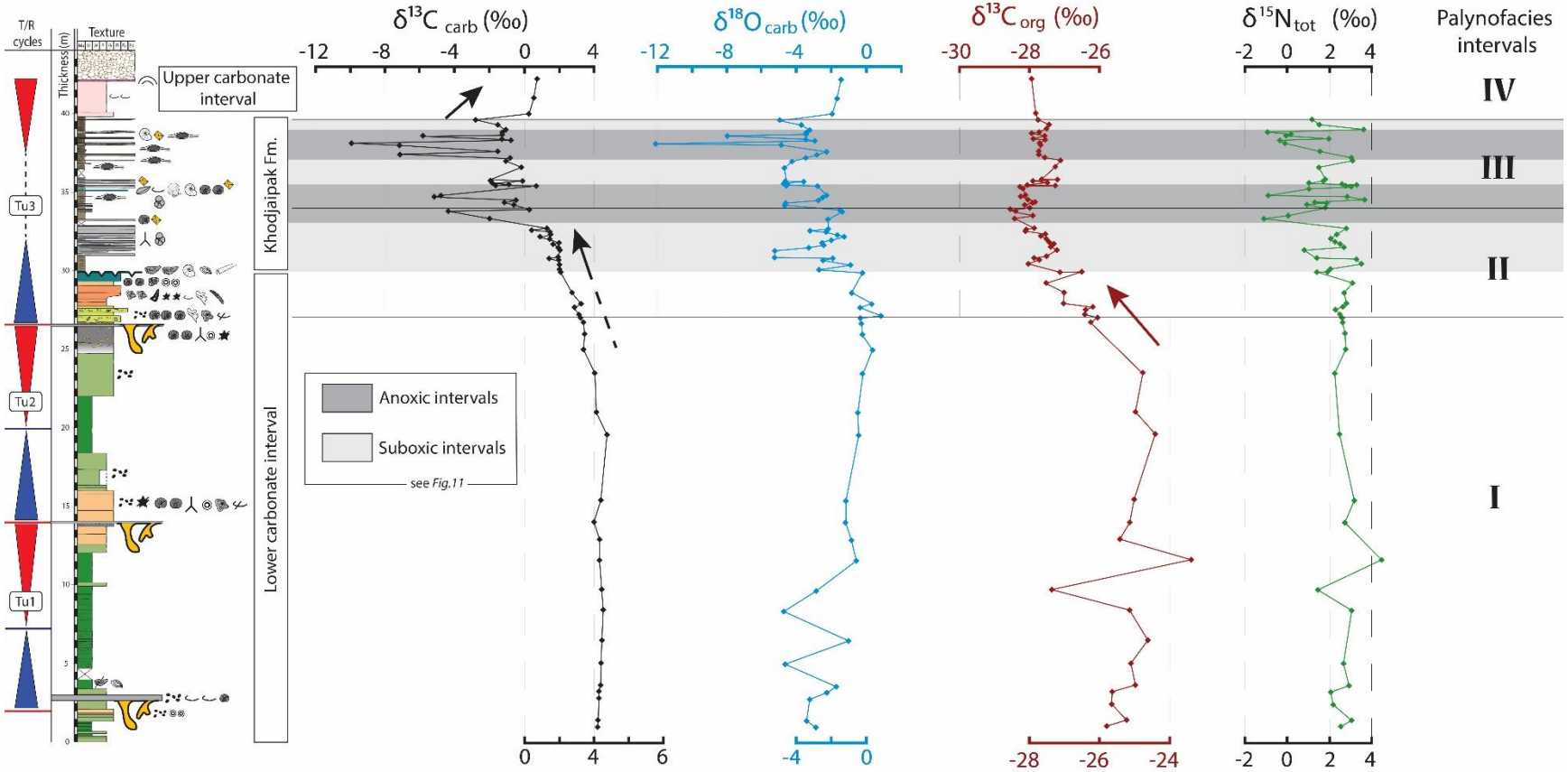

Fig. 9: Vertical evolution of organic ($\delta^{13}C_{org}$), inorganic ($\delta^{13}C_{carb}$ and $\delta^{18}O_{carb}$) and total ($\delta^{15}N_{tot}$) isotope ratio along the Tubiegatan section.

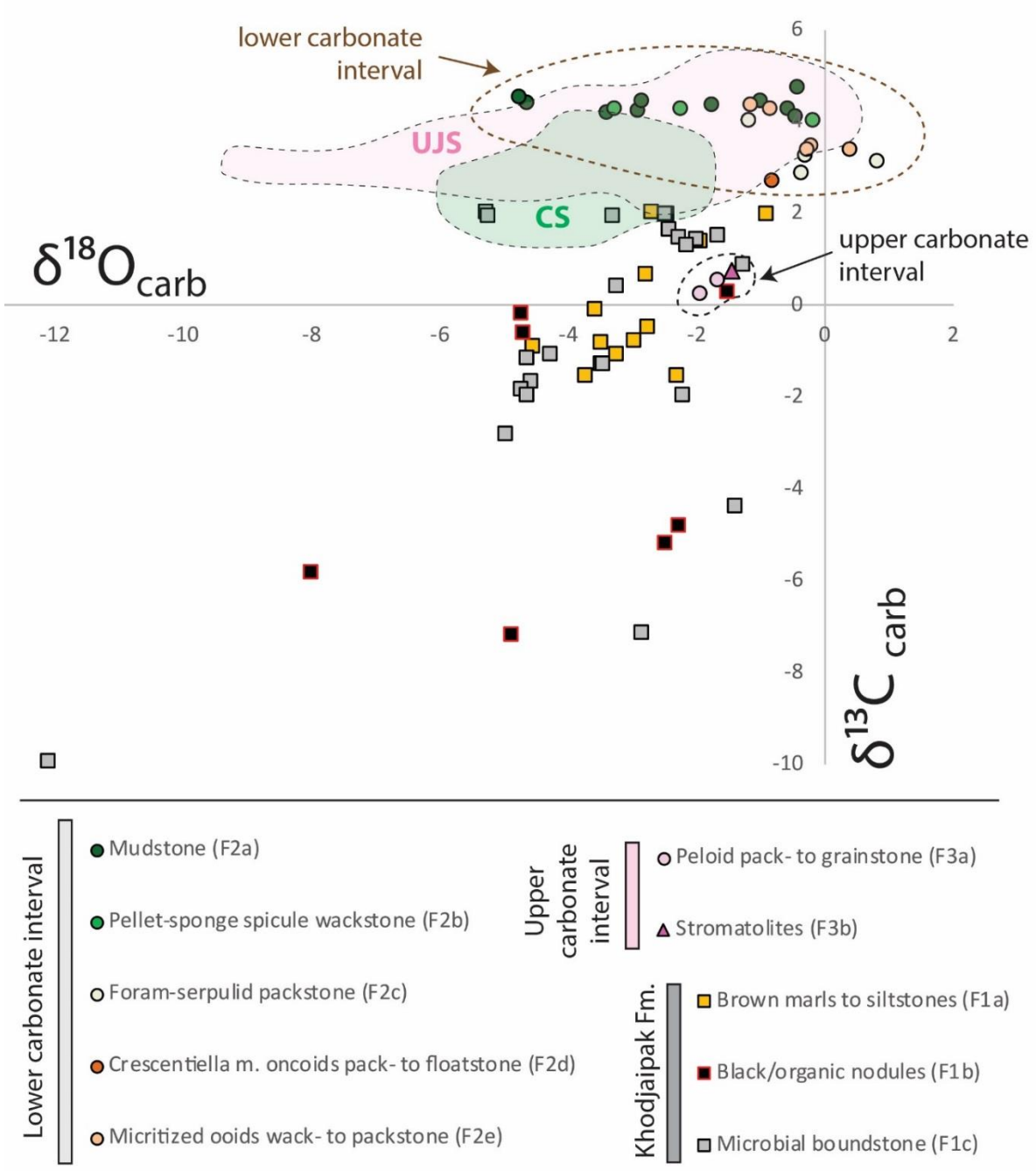

Fig. 10: $\delta^{13}C_{carb}$-$\delta^{18}O_{carb}$ cross-plots for the Tubiegatan section: Khodjaipak Fm., lower and upper carbonate intervals. The range of values for the south west Gissar platform carbonates (Callovian Sequence in green; Upper Jurassic Sequence in pink) are indicated.

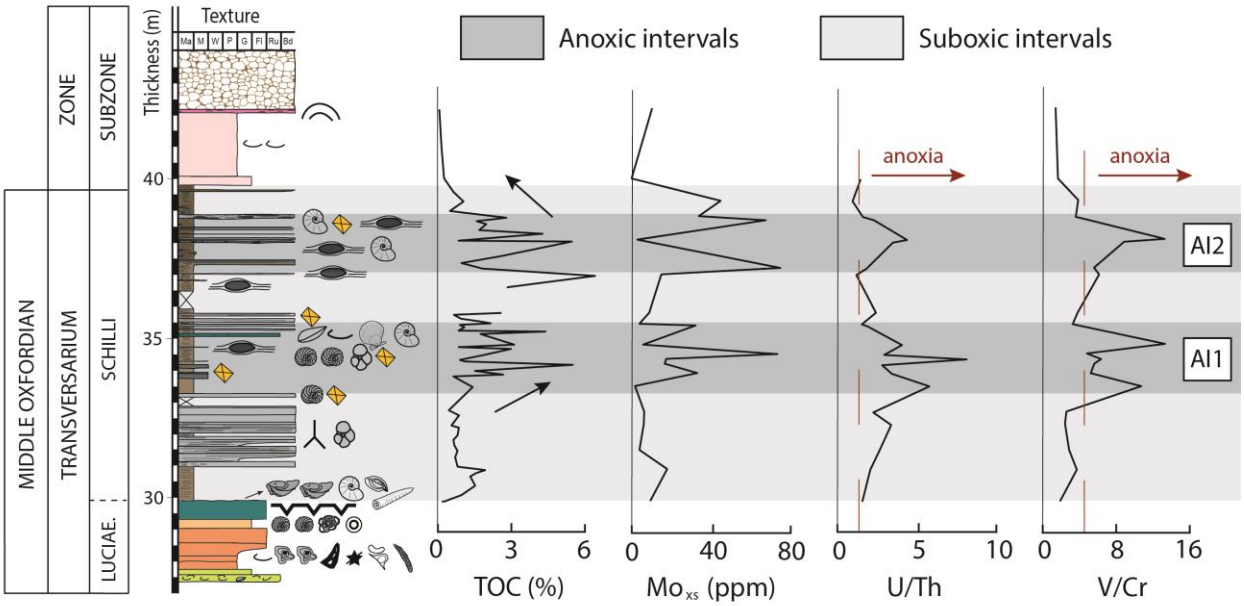

Fig. 11: Vertical evolution of TOC, Mo_{xs} and some trace metal elemental ratios: U/Th and V/Cr along the Khodjaipak Fm. Within grey intervals (AI1 and AI2), the ratios point to anoxic conditions.

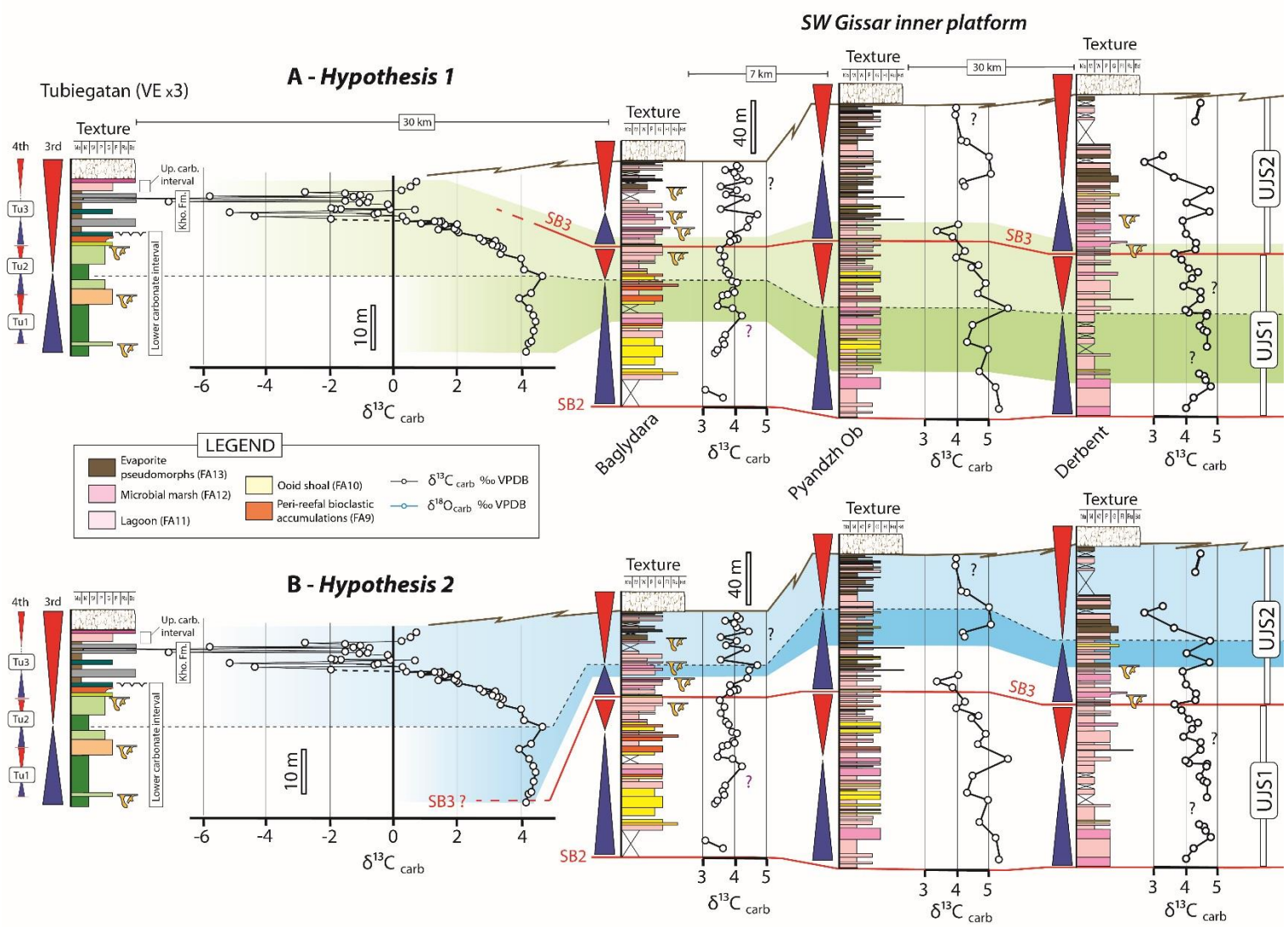

Fig. 12: Two correlation hypotheses between the Tubiegatan section and the south-west Gissar platform, based on the $\delta^{13}C_{carb}$ and the sequence stratigraphy.

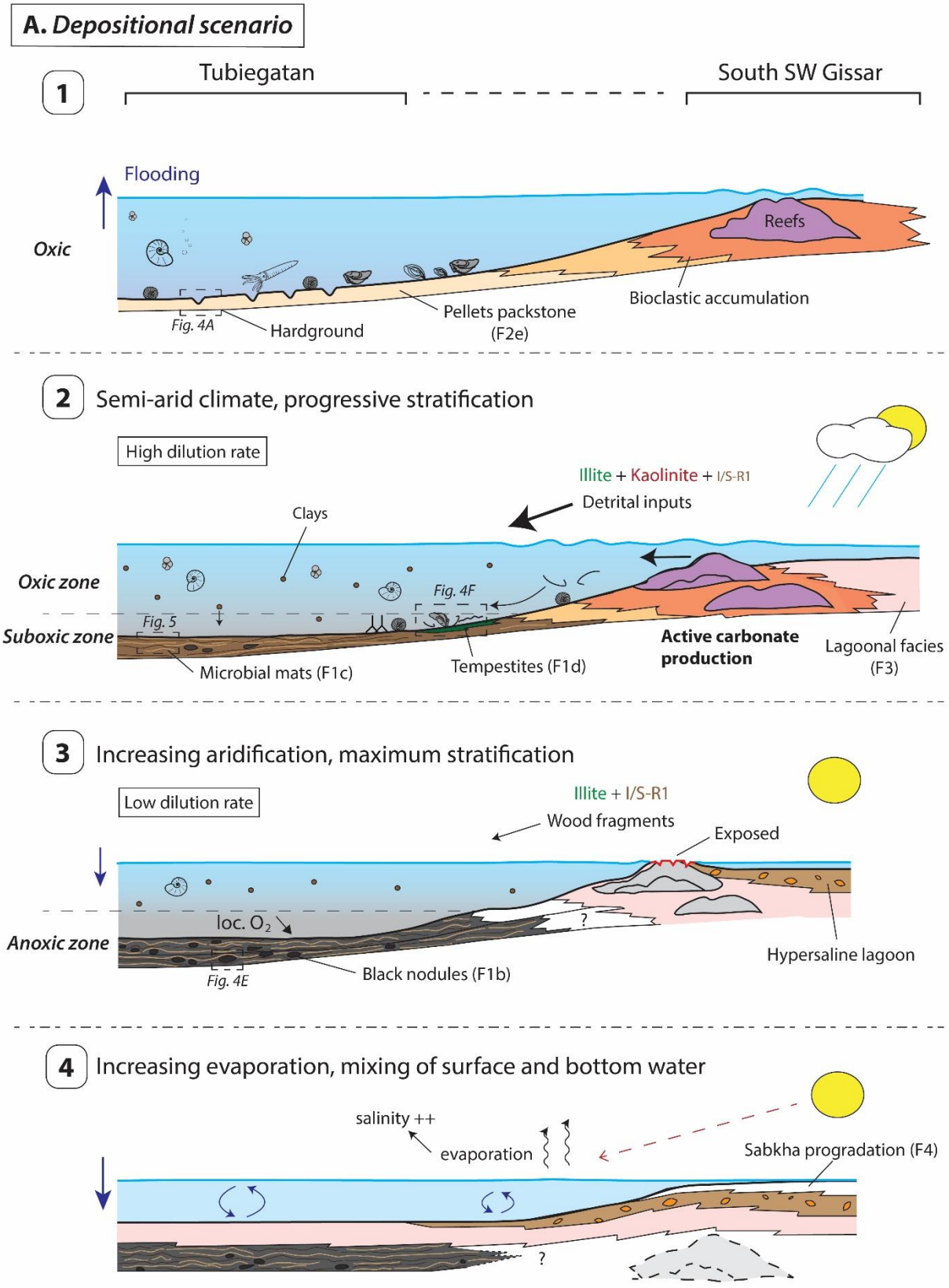
A. Depositional scenario
1
Tubiegatan
South SW Gissar
Flooding
Oxic
Reefs
Bioclastic accumulation
Fig. 4A
Hardground
Pellets packstone
(F2e)
2
Semi-arid climate, progressive stratification
High dilution rate
Illite + Kaolinite + I/S-R1
Detrital inputs
Clays
Oxic zone
Fig. 4F
Fig. 5
Suboxic zone
Active carbonate
production
Lagoonal facies
(F3)
Microbial mats (F1c)
Tempestites (F1d)
3
Increasing aridification, maximum stratification
Low dilution rate
Illite + I/S-R1
Wood fragments
Exposed
loc. O2
Anoxic zone
?
Hypersaline lagoon
Fig. 4E
Black nodules (F1b)
4
Increasing evaporation, mixing of surface and bottom water
salinity ++
evaporation
Sabkha progradation (F4)
?

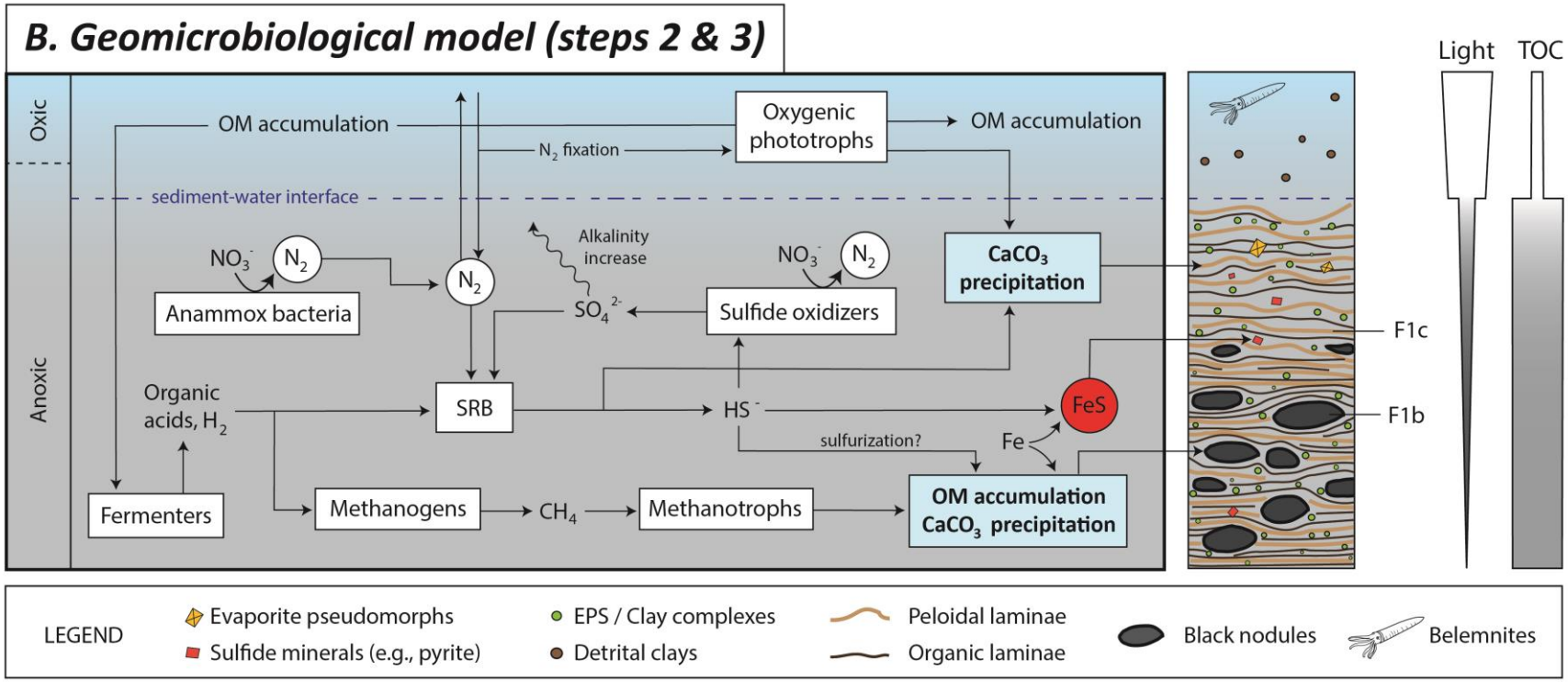

Fig. 13: (A) Depositional scenario and **(B)** geomicrobiological model for the Khodjaipak Fm. in the Tubiegatan area, and relationship with the SW Gissar carbonate platform.

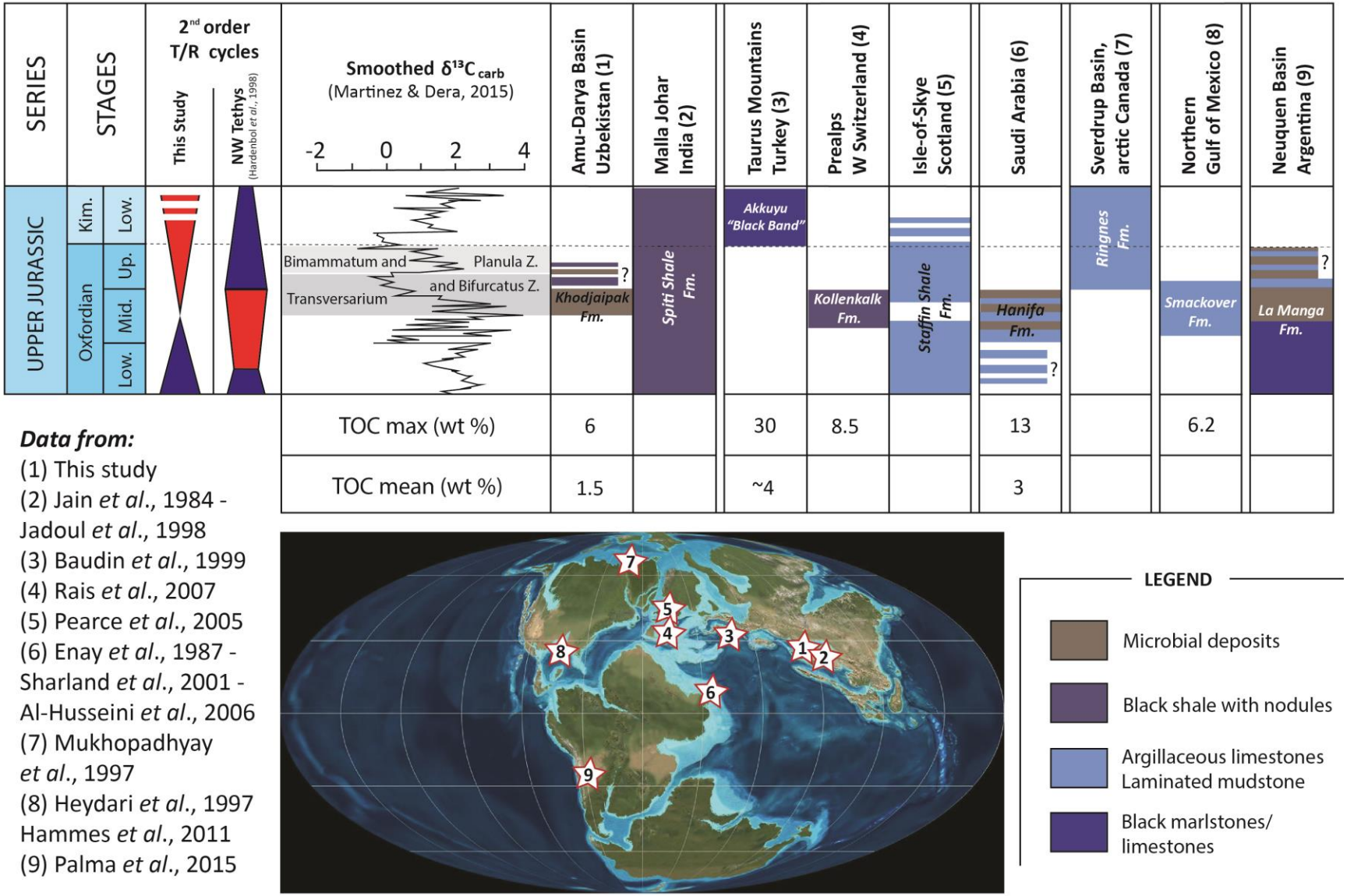

Fig. 14: Age, composition and distribution of the OM-rich sedimentary formation during the Oxfordian-Early Kimmeridgian period. The second-order NW Tethyan T/R cycles are from Hardenbol et al, 1998. The smoothed δ^{13}Ccarb curve is from Martinez and Dera, 2015.

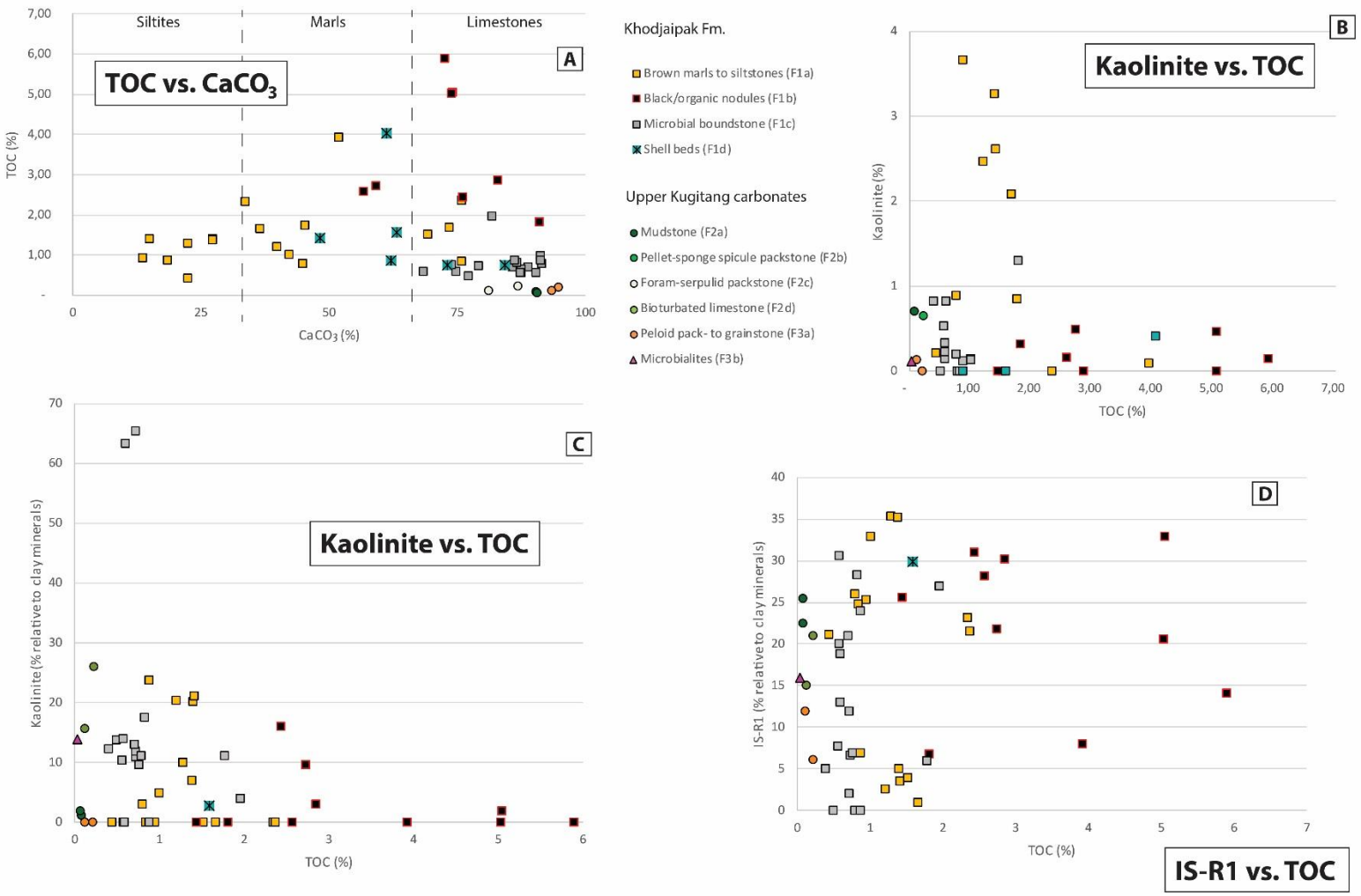

Fig. S1: A) Plot of $CaCO_3$ vs. TOC values for the Tubiegatan samples. Note that the highest values are associated to carbonate samples. **B-C)** Kaolinite vs. TOC: **(B)** percentage of kaolinite relative to bulk rock and **(C)** percentage of kaolinite relative to the clay fraction. **D)** R1-type illite-smectite mixed-layer (IS-R1) vs. TOC. The percentage of IS-R1 is relative to the clay fraction.

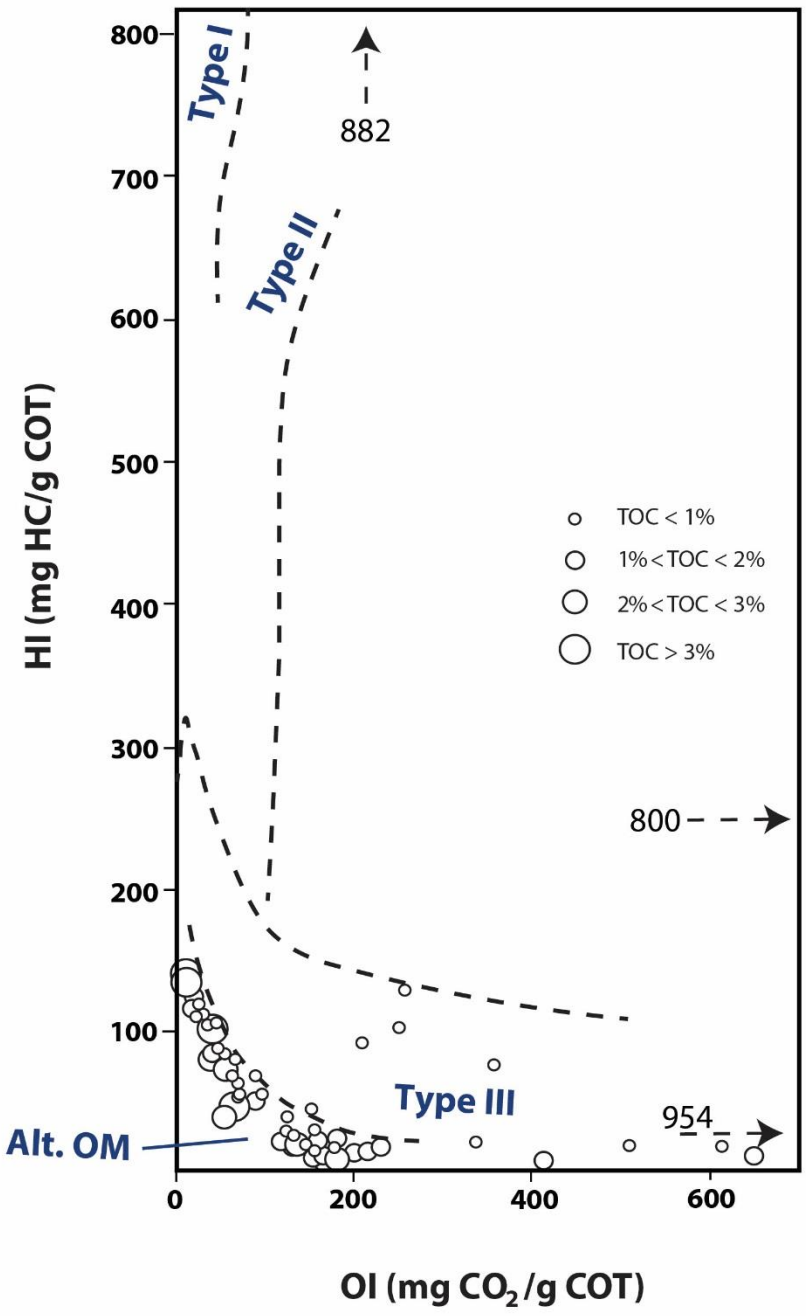

Fig. S2: Van Krevelen diagram: Hydrogen index (HI) vs. oxygen index (OI).

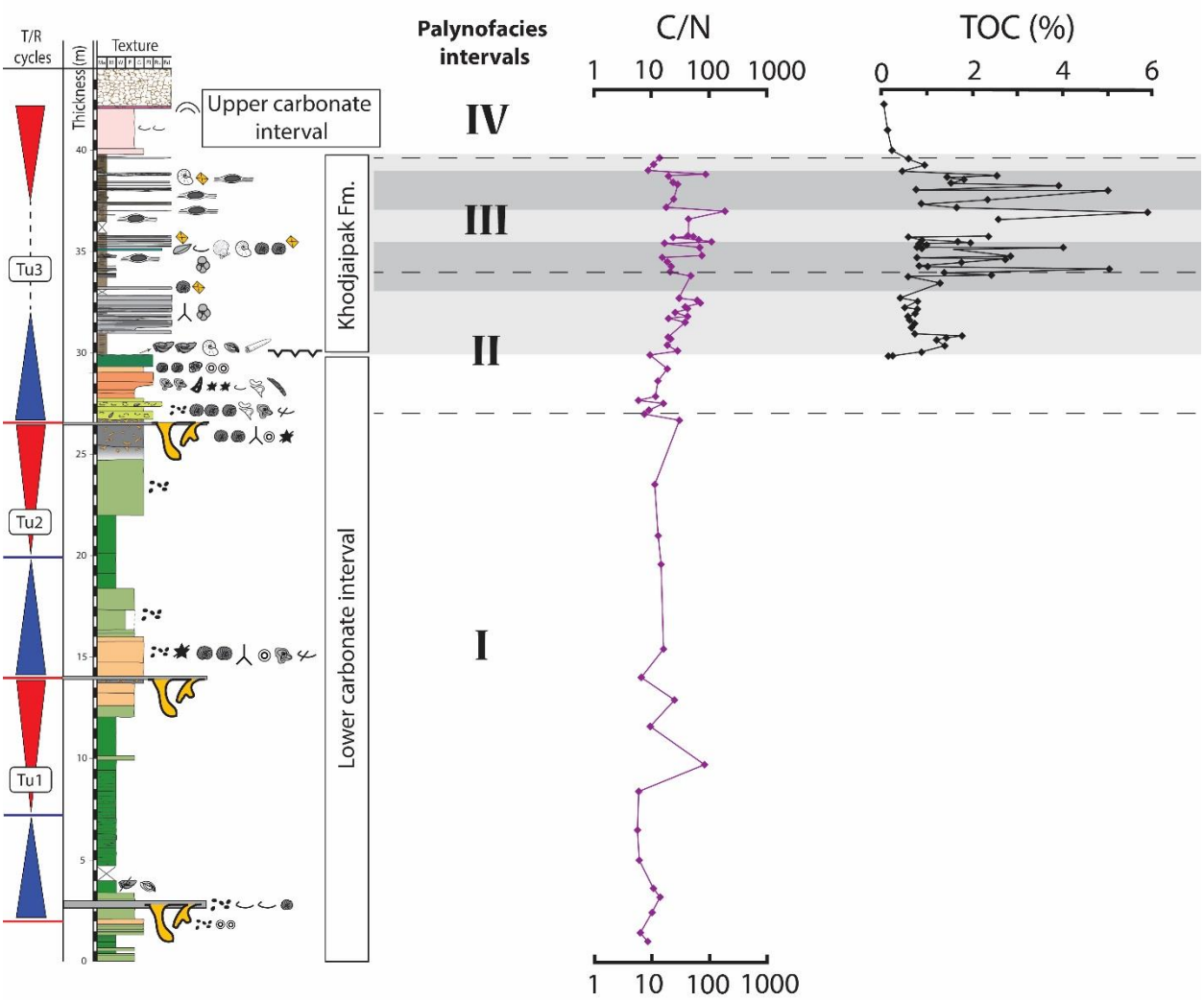

Fig. S3: Vertical evolution of the C/N ratio.